Article

INTERNATIONAL JOURNAL OF DAMAGE MECHANICS

International Journal of Damage Mechanics
0(0) 1–44

DOI: 10.1177/10567895211019065
journals.sagepub.com/home/ijd


A convex anisotropic damage model based on the compliance tensor

Johannes Görthofer[1], Matti Schneider[1], Andrew Hrymak[2] and Thomas Böhlke[1]

Abstract

This work is devoted to anisotropic continuum-damage mechanics in the quasi-static, isothermal, small-strain setting. We propose a framework for anisotropic damage evolution based on the compliance tensor as primary damage variable, in the context of generalized standard models for dissipative solids. Based on the observation that the Hookean strain energy density of linear elasticity is jointly convex in the strain and the compliance tensor, we design thermodynamically consistent anisotropic damage models that satisfy Wulfinghoff's damage-growth criterion and feature a convex free energy. The latter property permits obtaining mesh-independent results on component scale without the necessity of introducing gradients of the damage field. We introduce the concepts of stress-extraction tensors and damage-hardening functions, implicitly describing a rigorous damage-analogue of yield surfaces in elasto-plasticity. These damage surfaces may be combined in a modular fashion and give rise to complex damage-degradation behavior. We discuss how to efficiently integrate Biot's equation implicitly, and show how to design specific stress-extraction tensors and damage-hardening functions based on Puck's anisotropic failure criteria. Last but not least we demonstrate the versatility of our proposed model and the efficiency of the integration procedure for a variety of examples of interest.

Keywords

Continuum damage mechanics, anisotropic damage model, compliance evolution, generalized standard material, convex dissipation potential, Puck damage functions

[1]Institute for Engineering Mechanics, Karlsruhe Institute of Technology (KIT), Karlsruhe, Germany
[2]Department of Chemical and Biochemical Engineering, University of Western Ontario (UWO), Ontario, Canada

Corresponding author:
Thomas Böhlke, Institute of Engineering Mechanics, Karlsruhe Institute of Technology (KIT), Kaiserstraße 10, 76131 Karlsruhe, Germany.
Email: thomas.boehlke@kit.edu

Introduction

State of the art

Damage mechanics describes the progressive degradation of the elastic stiffness of materials upon loading, and is typically attributed to growing voids or cracks on a lower length scale (Lemaitre, 1996), see Figure 1. There are two predominant approaches to continuum damage-mechanics (Krajcinovic, 1984; Lemaitre and Chaboche, 1990). The first approach accounts for the origin of damage on a lower length scale in terms to micromechanics (Fitoussi et al., 1996; Guo et al., 1997), see also Section 3 in Krajcinovic (1989) for an early account. With qualitative predictions in mind, the second strategy is of phenomenological nature. After selecting a suitable damage variable (or a collection thereof), suitable kinetic laws are postulated taking continuum thermodynamics into account, Section 4 in Krajcinovic (1989).

The micromechanics-based approach to damage mechanics takes the damage mechanisms on a lower scale into account and is still subject of current research, for instance concerning mesh-size objective modeling (Liang et al., 2018), a coupling to model-order reduction (Bhattacharyya et al., 2020) or accounting for micro-computed tomography data (Luo et al., 2020). Micromechanics-informed damage models permit taking the stochastics on the microscale into account naturally, e. g., for progressive fiber breakage in fiber-reinforced composites (Ju and Wu, 2016; Wu and Ju, 2017), interfacial transition-zone effects (Chen et al., 2018), uncertainty in the elastic moduli of fiber-reinforced concrete (Liu et al., 2020), localized microcracks (Li et al., 2020) or random loading in fatigue processes (Franko et al., 2017). Another advantage concerns modeling the unilateral character of brittle damage, i. e., a different damaging behavior under tension compared to compression (Goidescu et al., 2015; Zhang et al., 2019), and accounting for interface debonding (Pupurs and Varna, 2017; Schemmann et al., 2018b; Yang et al., 2020). However, care has to be taken as homogenization and localization are incompatible (Gitman et al., 2007), in general, i.e., upon localization, the volume elements considered will not be representative for the effective mechanical behavior (Drugan and Willis, 1996; Hill, 1963; Kanit et al., 2003).

As an alternative to micromechanics-type strategies, phenomenological approaches to continuum-damage mechanics may be pursued. In a first step, a (scalar- or tensor-valued) damage variable is selected which describes the reduction of the effective cross-section of a typical material sample undergoing material degradation (Gurson, 1977; Voyiadjis, 2015). Then, suitable kinetic laws are postulated on the basis of continuum thermodynamics (Hansen and Schreyer, 1994; Simo and Ju, 1987).

The tensor order of the damage variable naturally distinguishes different phenomenological damage models. Even today, the classical scalar isotropic damage variable serves as a reliable

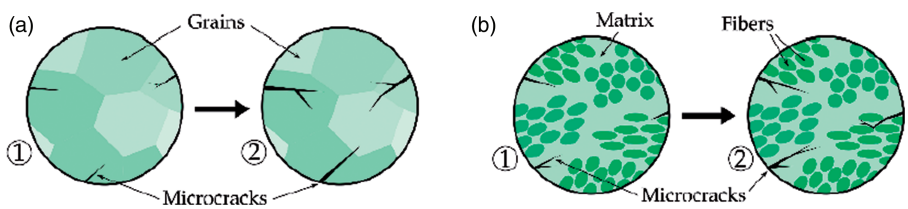

Figure 1. Schematics of microstructures with growing microscopic cracks, passing from state ① to state ②, similar to Fassin et al. (2019). Growing microcracks induce a reduction of the effective stiffness. (a) Polycrystalline microstructure. (b) Microstructure composed of fiber bundles.

workhorse with numerous applications including cast steel with pores (Yan et al., 2020), concrete (Li and Wu, 2018), rocks (Liu et al., 2018; Xu et al., 2018), framed structures (Yang et al., 2017), unidirectional glass fiber-reinforced plastic composite plies (Sharma and Daggumati, 2020), fibrous composite laminae (Abu-Farsakh and Asfa, 2020), notched epoxy resin specimens (Rahimi et al., 2020) and steel-fiber reinforced concrete (Moradi et al., 2020).

Damage variables with higher tensor order permit modeling an emerging anisotropy of damage. As working with second-order tensors comes naturally to disciples of continuum mechanics, it is not surprising that second-order damage-tensors (Murakami and Ohno, 1981) are used frequently in continuum damage-mechanics. Recent applications include concrete (Desmorat, 2016; Wardeh and Toutanji, 2017), metal-forming processes (Nasab and Mashayekhi, 2019), rock materials (Wang and Xu, 2020), composite fabrics and laminated panels (Wei et al., 2020) and composite laminates (Okabe et al., 2018; Onodera and Okabe, 2020). Second-order damage-tensors are always orthotropic w. r. t. their eigenbasis, limiting their degree of generality. More often than not, such a limitation is interpreted as a feature, and specific orthotropic damage models are developed, for instance for brittle materials (Kim et al., 2016), in elastoplastic and finite-strain damage coupling (Ganjiani, 2018; Reese et al., 2021), or for ceramic-matrix composites (Alabdullah and Ghoniem, 2020).

As continuum damage-models primarily seek to describe a loss of stiffness due to emerging defects in solids, using a fourth-order damage-tensor (Chaboche, 1981), the same tensor order as the stiffness tensor, appears reasonable. In Section 4.3.4, Krajcinovic (1989) even notes that "an appropriate description of damage [...] must involve at least a fourth-rank tensor." This idea was pursued for the stiffness or compliance tensors as the primary damage variable (Dougill, 1976; Ortiz, 1985; Ortiz and Popov, 1982), also coupled to plasticity (Ju, 1989; Simo and Ju, 1987; Yazdani and Schreyer, 1990). We refer to Zhang and Cai (2010) for a modern account of anisotropic damage mechanics. However, some care has to be taken when working with tensor-valued damage variables due to possible inconsistencies arising for complex non-radial loading-unloading scenarios, see Simon et al. (2017).

The unilateral character of pores and cracks (see Figure 1) often leads to a tension-compression asymmetry of the material behavior upon damage loading, see Chaboche (1993) for a discussion. To incorporate the latter effect in phenomenological models, one may introduce different damage variables for the tensile and the compressive regime (Cicekli et al., 2007; Ramtani et al., 1992). For three-dimensional stress states, spectral decompositions of either the strain or the stress tensor may form the basis of continuum damage models that differentiate between damage evolution due to tension and compression (Ladeveze and Lemaitre, 1984; Ortiz, 1985).

Whenever damage models exhibit a softening behavior, their use in a continuum formulation leads to an ill-posed problem due to localization effects (Lemaitre, 1986), which is reflected by strongly mesh-dependent results in numerical simulations (De Borst, 1996). Countermeasures in the framework of local damage models were investigated (Becker et al., 1988; Beremin et al., 1983; Tvergaard, 1982). Non-local formulations (Bažant, 1991; Belytschko et al., 1986) prevent the localization responsible for the ill-posedness, and may be realized by an explicit convolution with a tapering function (Pijaudier-Cabot and Bažant, 1987), by augmenting the damage evolution equation by an elliptic differential operator (Aifantis, 1984) or by employing a gradient-enhanced formulation (Abu Al-Rub and Voyiadjis, 2009; Brünig and Ricci, 2005; Germain et al., 2007), which may also be coupled to Hamilton's least-action principle (Junker et al., 2019, 2021). As long as the softening is not too pronounced, existence of results for non-local damage models (Thomas and Mielke, 2010) may be established. However, except for specific models (Roubíček, 2009; Susu, 2017), uniqueness (and, thus, well-posedness) cannot be ensured. For a review on ill-posedness

due to localization problems and appropriate regularization methods, the reader is referred to Forest et al. (2004). Also, for a general overview on continuum damage-mechanics and further literature, the reader may consult the books of Murakami (2012) and of Voyiadjis (2015).

Oftentimes, the ill-posedness of local damage models is taken for granted, and appropriate countermeasures are taken. A charming strategy takes a conventional local damage model with softening (but sufficient growth at infinity), and applies relaxation techniques (Balzani and Ortiz, 2012; Schmidt and Balzani, 2016; Schwarz et al., 2021), which are typically used for studying solids with emerging microstructure. When describing stable damage processes, these countermeasures should not be neccesary, however. Indeed, for a moderate degree of loading, localization is excluded, and manifests only at a specific turning point in loading level. For component-scale simulations, this loading level is not readily apparent, and depends on the specimen geometry via solving the equations of continuum mechanics. To sum up and loosely speaking, we know that local damage models are perfectly reasonable up to a specific level of loading, but we do not know this level in advance. Thus, interest arose to design damage models which give rise to a meaningful response for the entire range of loading, and which are intended to be complemented by a classical failure criterion.

Contributions and organization of this article

We contribute to phenomenological continuum damage-mechanics with a tensorial damage variable. We advocate using the full compliance tensor as a rather natural and observable damage variable, liberating the engineer of the burden of selecting the appropriate damage variable in advance, permitting her to focus the attention on appropriate kinetic laws. Thus, when it comes to continuum damage-mechanics of phenomenological type, the proposed framework is as ab-initio as possible, since only the evolution of the damage surface in stress space needs to be identified.

The compliance tensor has been used as the primary damage variable before (Baranger, 2018; Ladevèze, 1983, 2002; Ladevèze et al., 2014). Yet, this approach has not yet entered the main stream of damage-modeling frameworks. Our theoretical contributions to compliance-based damage models are actually twofold. For a start, we point out that the standard Hookean strain energy density, regarded as a function of the strain tensor and the full compliance tensor, is de facto jointly convex in both arguments. This result is surprising, and we are not aware of an account in the literature (although we sincerely believe that others have presumably noticed this fact before without stating it explicitly, see Thomas and Mielke (2010) for a special case).

Based on the compliance tensor, we develop a simple, modular framework for anisotropic damage mechanics. The framework provides the working engineer with a number of options which we believe to be of advantage. Indeed, due to the convexity property of the Hookean elastic energy, it is possible to develop a purely hardening damage-mechanics modeling-framework, where localization does not become an issue. Very much, there are materials which show a purely damage-hardening material response prior to sudden and brutal failure, e.g., Sheet Molding Compound (SMC) composites (Anagnostou et al., 2018; Fitoussi et al., 1996, 1998) comprising an unsaturated polyester-polyurethane hybrid (UPPH) resin (Kehrer et al., 2018; Schemmann et al., 2018a; Trauth et al., 2017) reinforced by glass fibers (Görthofer et al., 2019; Meraghni and Benzeggagh, 1995; Schemmann et al., 2018c).

Of course, the modeling framework is not restricted to damage-hardening, but may be adapted to softening in a straightforward manner. However, the latter scenario is rather classical in continuum damage-mechanics, and we decided to work out the details of a hardening framework in the paper at hand, essentially due to our desire to model SMC materials.

To highlight the simplicity of our proposed compliance-type damage modeling framework, we present a first-principles development in the context of generalized standard models (GSMs) for dissipative solids (Halphen and Nguyen, 1975) and discuss the efficient resolution of the evolution equations in a predictor-corrector framework.

Our second contribution concerns a design methodology for the damage surfaces which draws upon similar approaches in (associative) elastoplasticity (Bertram, 2011; Chaboche, 2008; McDowell, 2008), but takes failure criteria and multiple damage surfaces (Bakhshan et al., 2018; Jin and Arson, 2018; Khayyam Rayeni et al., 2020) into account. More precisely, building upon Puck's anisotropic failure criteria developed for continuously reinforced polymers (Knops, 2008; Puck and Schürmann, 2002), we design specific damage-extraction tensors and damage-activation functions which present a flexible arsenal of tools that, taking the individual damaging mechanisms into consideration, permit building up an accurate and fully anisotropic continuum damage model.

For anisotropic damage models not to be judged as *purely academic*, it is of utmost importance to establish links to experimental data and to compare it to (dis)similar modeling approaches. After conducting computational investigations which clarify the influence of the different model parameters on the damage evolution and expose the developing elastic anisotropy upon loading, we study a plain-weave mesostructure of a woven carbon-fiber reinforced thermoset investigated by Simon et al. (2017). We show that the convex modeling framework permits reproducing the effective mechanical behavior of the individual tows and the composite quantitatively within the loading range of interest.

Notation

We follow a direct tensor notation throughout the text, representing vectors and tensors by their components or using matrix representations (in an orthonormal basis) only when necessary. Vectors and second-order tensors are denoted by lower case and upper case bold letters, respectively (e.g., $\boldsymbol{a}$ and $\boldsymbol{A}$). Fourth-order tensors are denoted by, e.g., $\mathbb{A}, \mathbb{B}$. Scalars and arrays of quantities are represented by non-bold letters (e.g., H, w or z). The transposition of a vector and second-order tensor reads $\boldsymbol{a}^{\mathrm{T}}$ and $\boldsymbol{A}^{\mathrm{T}}$, respectively. The principal transposition of a fourth-order tensor is denoted via $\mathbb{A}^{\mathrm{T_M}}$ and the left and right transpositions are $\mathbb{A}^{\mathrm{T_L}}$ and $\mathbb{A}^{\mathrm{T_R}}$. The linear mappings induced by second-order and fourth-order tensors are written as $\boldsymbol{a} = \boldsymbol{C}\boldsymbol{b}$ and $\boldsymbol{A} = \mathbb{C}[\boldsymbol{B}]$, respectively. The composition of two second-order or two fourth-order tensors is denoted by $\boldsymbol{A}\boldsymbol{B}$ and $\mathbb{A}\mathbb{B}$. The Frobenius inner product is denoted by $\boldsymbol{A} \cdot \boldsymbol{B} = \mathrm{tr}(\boldsymbol{A}\boldsymbol{B}^{\mathrm{T}})$. The tensor product is symbolized by $\otimes$. Its symmetrized version $\otimes_{\mathrm{S}}$ is defined via $\boldsymbol{a} \otimes_{\mathrm{S}} \boldsymbol{b} = (\boldsymbol{a} \otimes \boldsymbol{b} + \boldsymbol{b} \otimes \boldsymbol{a})/2$. We introduce the abbreviation $\boldsymbol{a}^{\otimes n} = \boldsymbol{a} \otimes \boldsymbol{a} \ldots \otimes \boldsymbol{a}$ (n repetitions). The material time derivative of a quantity w is expressed as $\dot{w} = \mathrm{d}w/\mathrm{d}t$. We denote by $\mathrm{Sym}(d)$ the space of symmetric second-order tensors on $\mathbb{R}^d$. The unit sphere in $\mathbb{R}^3$ reads S^2. The vector space of fourth-order tensors with minor symmetries ($\mathbb{A} = \mathbb{A}^{\mathrm{T_L}}$, $\mathbb{A} = \mathbb{A}^{\mathrm{T_R}}$) is written as $L(\mathrm{Sym}(d))$, whereas $\mathrm{Sym}(\mathrm{Sym}(d))$ denotes those-fourth order tensors that have minor and major symmetries ($\mathbb{A} = \mathbb{A}^{\mathrm{T_M}}$). In general, details on further spaces of interest, domains of definition and corresponding explicit expressions are given upon their first appearance.

A compliance-based anisotropic damage model

A convex standard model for anisotropic damage

We will describe the damage model, in a small-strain and isothermal setting, as a generalized standard model (GSM) (Halphen and Nguyen, 1975), whose framework we briefly recall. In addition to

the symmetric $d \times d$ infinitesimal strain tensor $\boldsymbol{\varepsilon} \in \mathrm{Sym}(d)$, where $d = 2, 3$ denotes the dimension of the ambient space, a (Banach) space $\mathcal{Z}$ of internal variables is postulated. Furthermore, a free energy (density)

$$w : \mathrm{Sym}(d) \times \mathcal{Z} \to \mathbb{R}, \quad (\boldsymbol{\varepsilon}, z) \mapsto w(\boldsymbol{\varepsilon}, z), \tag{2.1}$$

a continuously differentiable function of the strain tensor $\boldsymbol{\varepsilon}$ and the internal variables $z \in \mathcal{Z}$, and a force potential $\Phi^* : \mathcal{Z}' \to [0, \infty]$, a lower semicontinuous, non-negative and convex function on the continuous dual space $\mathcal{Z}'$ satisfying $\Phi^*(0) = 0$, are introduced. To ensure thermodynamic consistency, the Clausius-Duhem inequality (CDI), see Chapter 13 in Haupt (2000),

$$0 \overset{!}{\leq} \boldsymbol{\sigma} \cdot \dot{\boldsymbol{\varepsilon}} - \frac{\mathrm{d}}{\mathrm{d}t}[w(\boldsymbol{\varepsilon}, z)] \equiv \left[\boldsymbol{\sigma} - \frac{\partial w}{\partial \boldsymbol{\varepsilon}}(\boldsymbol{\varepsilon}, z)\right] \cdot \dot{\boldsymbol{\varepsilon}} - \frac{\partial w}{\partial z}(\boldsymbol{\varepsilon}, z) \cdot \dot{z}, \tag{2.2}$$

where $\dot{z} \equiv \mathrm{d}z/\mathrm{d}t$ denotes the material time derivative of the internal variables, needs to be satisfied. Associated to a current equilibrium state $(\boldsymbol{\varepsilon}, z)$ of a hyperelastic material, the Cauchy stress tensor $\boldsymbol{\sigma} \in \mathrm{Sym}(d)$ is defined (Halphen and Nguyen, 1975; Miehe, 2002) by

$$\boldsymbol{\sigma} = \frac{\partial w}{\partial \boldsymbol{\varepsilon}}(\boldsymbol{\varepsilon}, z). \tag{2.3}$$

For a prescribed loading path $\boldsymbol{\varepsilon} : [0, T] \to \mathrm{Sym}(d)$ on a given interval of time and the initial condition $z(0) = z_0$ for some $z_0 \in \mathcal{Z}$, the evolution of the internal variables is governed by Biot's (dual) equation

$$\dot{z} \in \partial \Phi^* \left(-\frac{\partial w}{\partial z}(\boldsymbol{\varepsilon}, z) \right), \tag{2.4}$$

where $\partial \Phi^*$ denotes the subdifferential of the convex function Φ^*

$$\partial \Phi^*(\xi) = \left\{ z \in \mathcal{Z} \,|\, \Phi^*(\tilde{\xi}) - \Phi^*(\xi) \geq (\tilde{\xi} - \xi) \cdot z \quad \text{for all} \quad \tilde{\xi} \in \mathcal{Z}' \right\}, \tag{2.5}$$

a subset of $\mathcal{Z}'$, see Borwein and Lewis (2006) for details. Due to these definitions, see Halphen and Nguyen (1975), generalized standard materials are automatically thermodynamically consistent. Indeed, by Biot's (dual) equation (2.4),

$$\Phi^*(0) - \Phi^*(\xi) \geq (0 - \xi) \cdot \dot{z} \quad \text{for} \quad \xi = -\frac{\partial w}{\partial z}(\boldsymbol{\varepsilon}, z) \tag{2.6}$$

holds. Using $\Phi^*(0) = 0$, rearranging the latter inequality yields

$$-\frac{\partial w}{\partial z}(\boldsymbol{\varepsilon}, z) \cdot \dot{z} \equiv \xi \cdot \dot{z} \geq \Phi^*(\xi) \geq 0, \tag{2.7}$$

i.e., the Clausius-Duhem inequality (2.2) holds in view of the definition of stress (2.3). As it drives the evolution of the internal variables, the quantity $\xi \equiv -\frac{\partial w}{\partial z}(\boldsymbol{\varepsilon}, z)$ is called driving force.

As internal variables z of our proposed continuum damage-mechanics model, we consider an elastic compliance tensor

$$\mathbb{S} \in \mathcal{S}_d = \left\{ \mathbb{S} \in \mathrm{Sym}(\mathrm{Sym}(d)) \,|\, \boldsymbol{\tau} \cdot \mathbb{S}[\boldsymbol{\tau}] > 0 \quad \text{for all} \quad \boldsymbol{\tau} \in \mathrm{Sym}(d) \backslash \{0\} \right\}, \tag{2.8}$$

and a general variable $q \in \mathcal{Q}$ which describes the shape and size of the damage surface, s. t.

$$z = (\mathbb{S}, q) \in \mathcal{S}_d \times \mathcal{Q}. \tag{2.9}$$

Notice that the set $\mathcal{S}_d$ of (positive definite) compliance tensors is *not* a linear space. Instead, it is an open, convex subset of the linear space of fourth-order tensors $\mathrm{Sym}(\mathrm{Sym}(d))$ with minor and major symmetries.

For a GSM, the CDI (2.2) will always be satisfied. However, we need to ensure that the (dual) Biot's equation (2.4) guarantees that $\mathbb{S}$ remains an element of $\mathcal{S}_d$, i.e., that the compliance tensor $\mathbb{S}$ remains positive definite. In contrast, the damage-surface variables we consider live in a linear space $\mathcal{Q}$ (which we deliberately keep abstract). For the specific models presented in the next section q is just a finite collection of scalar values. However, our arguments cover the more general case, accounting for vector- or tensor-valued damage-surface variables in a natural way.

The free energy (density) we consider is defined by

$$w : \mathrm{Sym}(d) \times \mathcal{S}_d \times \mathcal{Q} \to \mathbb{R}, \quad (\boldsymbol{\varepsilon}, \mathbb{S}, q) \mapsto w_e(\boldsymbol{\varepsilon}, \mathbb{S}) + h(q), \tag{2.10}$$

involving the Hookean elastic energy (density)

$$w_e : \mathrm{Sym}(d) \times \mathcal{S}_d \to [0, \infty), \quad (\boldsymbol{\varepsilon}, \mathbb{S}) \mapsto \frac{1}{2}\, \boldsymbol{\varepsilon} \cdot \mathbb{S}^{-1}[\boldsymbol{\varepsilon}], \tag{2.11}$$

and an energy (density) related to the progressive degradation of the material,

$$h : \mathcal{Q} \to \mathbb{R}, \quad q \mapsto h(q), \tag{2.12}$$

which we assume to be convex and continuously differentiable. Notice that the Hookean elastic energy w_e (2.11) is jointly convex in both variables and infinitely often differentiable. The latter property is immediate[1], as w_e depends on $\boldsymbol{\varepsilon}$ quadratically and the Neumann-series representation

$$(\mathbb{S} + \mathbb{L})^{-1} = \sum_{k=0}^{\infty} (-\mathbb{S}^{-1}\mathbb{L})^k \mathbb{S}^{-1}, \quad \mathbb{S} \in \mathcal{S}_d, \quad \mathbb{L} \in \mathrm{Sym}(\mathrm{Sym}(d)), \tag{2.13}$$

valid for sufficiently small $\mathbb{L}$, shows that w_e is even analytic. For the convexity, recall that a twice differentiable function defined on an open convex set is convex if and only if its Hessian is positive semidefinite everywhere, see Theorem 3.1.11 in Borwein and Lewis (2006). A direct computation shows that the Hessian admits the representation

$$D^2 w_e(\boldsymbol{\varepsilon}, \mathbb{S})[\boldsymbol{\xi}, \mathbb{L}] = \frac{1}{2} \left(\boldsymbol{\xi} - \mathbb{L}\mathbb{S}^{-1}[\boldsymbol{\varepsilon}] \right) \cdot \mathbb{S}^{-1} \left[\boldsymbol{\xi} - \mathbb{L}\mathbb{S}^{-1}[\boldsymbol{\varepsilon}] \right], \tag{2.14}$$

for $(\boldsymbol{\varepsilon}, \mathbb{S}) \in \mathrm{Sym}(d) \times \mathcal{S}_d$ and $(\boldsymbol{\xi}, \mathbb{L}) \in \mathrm{Sym}(d) \times \mathrm{Sym}(\mathrm{Sym}(d))$, see Appendix B. Any $\mathbb{S} \in \mathcal{S}_d$ is positive definite, and thus, the Hessian in equation (2.14) is non-negative. Consequently, the elastic energy is convex (but *not* strictly convex). As we assumed the energy h (2.12) to be continuously differentiable and convex, the smoothness and convexity properties of w_e imply that the free energy w (2.10) is continuously differentiable and convex, as well. Furthermore, the formula for the Cauchy stress (2.3) becomes

$$\boldsymbol{\sigma} = \frac{\partial w}{\partial \boldsymbol{\varepsilon}}(\boldsymbol{\varepsilon}, \mathbb{S}, q) \equiv \mathbb{S}^{-1}[\boldsymbol{\varepsilon}], \tag{2.15}$$

i.e., for a fixed compliance tensor $\mathbb{S}$, the stress-strain relationship reduces to Hooke's law. To conclude this paragraph, several remarks are in order.

1. Using the framework of generalized standard materials for phenomenological modeling of damage is classical. For instance, Hansen and Schreyer (1994) study a general tensor-valued damage variable coupled to plasticity in such a framework, apparently unaware of the connection.
2. In phenomenological continuum damage-mechanics, choosing the damage variable typically comes first, and the damage kinetics needs to be set up based on the resulting driving forces. Our approach frees the reader of an a priori selection of damage variable, and permits her to focus on the kinetics in terms of the quite natural stress-based driving force.
3. The compliance tensor has the attractive characteristic that it is a physical quantity which can be determined experimentally. Of course, determining all 21 independent parameters of a stiffness tensor in three spatial dimensions is a daunting task from an experimental perspective. Still, observability of the damage variable is not ensured for purely phenomenological damage vectors and tensors.
4. The compliance tensor has been used as a damage variable before (Ladevèze, 1983, 2002). However, its use seemed restricted to specific situations, e.g., damage modeling in ceramic-matrix composites (Baranger, 2018; Ladevèze et al., 2014). In this work, we advocate using the compliance tensor as the damage variable of choice in greater generality.
5. It is more than well-known that the Hookean energy (2.11) is convex in the strain tensor. It appears much less known that the Hookean energy is *jointly* convex in the strain *and* the compliance tensor. When coupled to an energy h which makes the condensed incremental potential strictly convex, the resulting framework produces an anisotropic damage model which does not permit localization. In particular, associated finite-element computations are not affected by mesh sensitivity induced by softening behavior. We do not want to argue against damage localization. Rather, we wish to add a powerful weapon to the arsenal of continuum damage-mechanics when it comes to modeling stable anisotropic damage phenomena.
6. In classical small-strain elasto(visco)plasticity the (visco)plastic strain $\boldsymbol{\varepsilon}_p \in \mathrm{Sym}(d)$ serves as an internal variable. The corresponding stored energy (density)

$$(\boldsymbol{\varepsilon}, \boldsymbol{\varepsilon}_p) \mapsto \frac{1}{2}\,(\boldsymbol{\varepsilon} - \boldsymbol{\varepsilon}_p) \cdot \mathbb{C}[\boldsymbol{\varepsilon} - \boldsymbol{\varepsilon}_p] \tag{2.16}$$

with a fixed stiffness tensor $\mathbb{C} = \mathbb{S}^{-1}$ is smooth and jointly convex in both arguments, but not strictly convex. The Hookean elastic stored energy function w_e (2.11) may be considered as a damage-analog of the elastic stored energy in classical elasto(visco)plasticity (2.16). The combined energy taking into account damage (2.11) and elasto(visco)plasticity (2.16) is jointly convex

in all variables. If plasticity is neglected ($\boldsymbol{\varepsilon}_p \equiv 0$) we recover the damage case and for a constant stiffness ($\mathbb{C} = \mathbb{S}^{-1} \equiv$ const.) we recover classical elasto(visco)plasticity. Such a model differs from the classical presentation, which is typically based on either strain or energy equivalence (Hansen and Schreyer, 1994; Sections 3.2.1 and 3.2.2).

7. If we regard the Hookean elastic stored energy function $(\boldsymbol{\varepsilon}, \mathbb{C}) \mapsto \frac{1}{2}\boldsymbol{\varepsilon} \cdot \mathbb{C}[\boldsymbol{\varepsilon}]$ as a function of the stiffness tensor $\mathbb{C}$, it will *not* be convex. Indeed, its Hessian at $(\boldsymbol{\varepsilon}, \mathbb{C})$ computes as

$$(\boldsymbol{\xi}, \mathbb{L}) \mapsto 2\boldsymbol{\xi} \cdot \mathbb{L}[\boldsymbol{\varepsilon}] + \boldsymbol{\xi} \cdot \mathbb{C}[\boldsymbol{\xi}], \tag{2.17}$$

which may become negative (take, for instance $\boldsymbol{\xi} = \boldsymbol{\varepsilon}$ and $\mathbb{L} = -\mathbb{C}$). This lack of convexity is the reason why it is so difficult to design convex damage models for stable damage processes. Using the compliance tensor eradicates these issues with the help of a nonlinear transformation.

8. For the thermodynamics considerations at the beginning of this section to be valid, the "interfacial" energy (2.12) need not be convex, see, for example, Govindjee et al. (1995). In particular, softening behavior can be modeled in the compliance-tensor framework, as well. In that case, for obtaining a well-defined boundary-value problem, damage localization has to be overcome, for instance by adding gradient terms of the variable q to the energy (2.12).
9. The presented model cannot distinguish tensile and compressive loading. Indeed, the driving force $\mathbb{T}$ (2.18) for the compliance evolution computes as

$$\mathbb{T} = -\frac{\partial w(\boldsymbol{\varepsilon}, \mathbb{S}, q)}{\partial \mathbb{S}} = -\frac{\partial w_e(\boldsymbol{\varepsilon}, \mathbb{S})}{\partial \mathbb{S}} = \frac{1}{2}\boldsymbol{\sigma} \otimes \boldsymbol{\sigma} \in \mathrm{Sym}(\mathrm{Sym}(d)), \tag{2.18}$$

which is insensitive to the involution $\boldsymbol{\sigma} \mapsto -\boldsymbol{\sigma}$. Thus, in order to extend our model to account for tension-compression asymmetry, the free energy w requires a modification, see Ladevèze and coworkers (Ladevèze, 1983, 2002; Ladevèze et al., 2014).

To finish presenting the two-potential model, a suitable force potential Φ^* needs to be provided, entering the evolution equation of the internal variables, see equation (2.4),

$$(\dot{\mathbb{S}}, \dot{q}) \in \partial\Phi^*(\mathbb{T}, \beta). \tag{2.19}$$

In the quasi-static setting targeting a rate-independent damage model, we describe the force potential Φ^* in terms of M continuously differentiable and convex damage functions $\phi_i : \mathrm{Sym}(\mathrm{Sym}(d)) \times \mathcal{Q}' \to \mathbb{R}$, i.e.,

$$\Phi^*(\mathbb{T}, \beta) = \begin{cases} 0, & \phi_i(\mathbb{T}, \beta) \leq 0 \quad \text{for all} \quad i = 1, \ldots, M, \\ +\infty, & \text{otherwise.} \end{cases} \tag{2.20}$$

Such a force potential gives rise to a quasi-static damage evolution in terms of an elastic domain defined by the functions ϕ_i, in strict analogy to associated elastoplasticity at small strains, see Chapter 5 in Simo and Hughes (1998). A schematic of the admissible region based on the force potential (2.20) with corresponding driving forces $\mathbb{T}$ and β is shown in Figure 2.

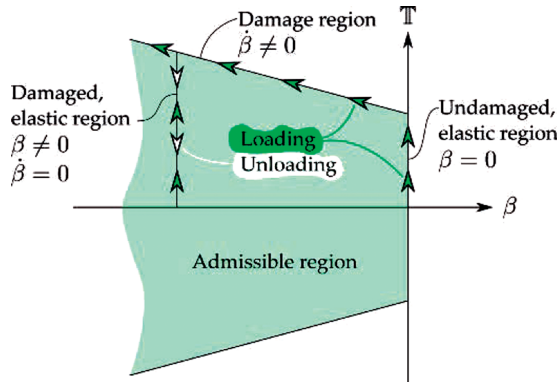

Figure 2. Schematic of the admissible elastic region in $(\mathbb{T}, \beta)$-space.

However, some care has to be exercised, as the elastic domain is defined in terms of the compliance driving-force $\mathbb{T}$, which takes the form $\mathbb{T} = \frac{1}{2}\boldsymbol{\sigma} \otimes \boldsymbol{\sigma}$ for the free energy w (2.10), in contrast to elastoplasticity, where the stress tensor $\boldsymbol{\sigma}$ (or a shifted version thereof) serves as the driving force. For the specific force potential Φ^* (2.20), Biot's (dual) equation (2.4) becomes

$$\dot{\mathbb{S}} = \sum_{i=1}^{M} \dot{\mu}_i \frac{\partial \phi_i(\mathbb{T}, \beta)}{\partial \mathbb{T}} \quad \text{and} \quad \dot{q} = \sum_{i=1}^{M} \dot{\mu}_i \frac{\partial \phi_i(\mathbb{T}, \beta)}{\partial \beta}, \tag{2.21}$$

involving the driving forces

$$\beta = -\frac{\partial w(\boldsymbol{\varepsilon}, \mathbb{S}, q)}{\partial q} \equiv -\frac{\partial h(q)}{\partial q} \in \mathcal{Q}' \tag{2.22}$$

for the evolution of the damage-surface variables q and consistency parameters $\mu_1, \ldots, \mu_M$ which obey the Karush-Kuhn-Tucker (KKT) conditions

$$\dot{\mu}_i \geq 0, \quad \phi_i(\mathbb{T}, \beta) \leq 0, \quad \dot{\mu}_i \, \phi_i(\mathbb{T}, \beta) = 0, \quad i = 1, \ldots, M. \tag{2.23}$$

To ensure that $\mathbb{S}$ remains in the set $\mathcal{S}_d$ of positive definite compliance tensors, a condition of the form

$$\frac{\partial \phi_i(\mathbb{T}, \beta)}{\partial \mathbb{T}} \geq 0 \quad \text{for all} \quad i = 1, \ldots, M, \tag{2.24}$$

on the damage functions ϕ_i is sufficient. The latter condition was established by Wulfinghoff et al. (2017) as a criterion any physically meaningful vectorial or tensorial continuum-damage model should satisfy. In our context, the compliance tensor $\mathbb{S}$ serves as the damage variable, and Wulfinghoff's criterion becomes "$\dot{\mathbb{S}} \geq 0$", i.e., $\dot{\mathbb{S}}$ is positive semidefinite.

To complete describing our model, we restrict the space of damage variables to $\mathcal{Q} = \mathbb{R}^M$, i.e., one scalar damage variable per damage-activation function ϕ_i. We define the damage-activation function to be

$$\phi_i : \mathrm{Sym}(\mathrm{Sym}(d)) \times \mathbb{R} \to \mathbb{R}, \quad (\mathbb{T}, \beta_i) \mapsto 2\mathbb{T} \cdot \mathbb{B}_i^2 - \sigma_{0,i}^2 + H_i \beta_i, \quad i = 1, \ldots, M, \tag{2.25}$$

involving a (fourth-order, dimension-free) damage-extraction tensor $\mathbb{B}_i \in L(\mathrm{Sym}(d))$ with minor and major symmetries, a damage-activation threshold $\sigma_{0,i}$ (analogous to the yield stress in elastoplasticity), and a positive parameter H_i with the dimensions of stress.

In principle, the damage-extraction tensor $\mathbb{B}_i$ need not have the major symmetry for equation (2.29) to make sense. In this non-symmetric case, the term $\mathbb{B}_i^2$ in equation (2.25) needs to be replaced by $\mathbb{B}_i^{\mathrm{T_M}} \mathbb{B}_i$ in terms of the transpose $\mathbb{B}_i^{\mathrm{T_M}}$ of the damage-extraction tensor $\mathbb{B}_i$. However, the framework (2.25) may be recovered by defining $\tilde{\mathbb{B}}_i = \sqrt{\mathbb{B}_i^{\mathrm{T_M}} \mathbb{B}_i}$. Thus, by restricting the damage-extraction tensor to have major symmetries we do not lose generality. Furthermore, as we consider the variable q_i to be dimensionless, the associated driving force β_i has dimensions of stress and the parameter H_i is necessary for dimensional reasons.

In any case, for the damage function (2.25) the condition (2.24) to fulfill Wulfinghoff's damage growth criterion, is automatically satisfied. Indeed, for any $i = 1, \ldots, M$, we obtain,

$$\boldsymbol{\tau} \cdot \frac{\partial \phi_i(\mathbb{T}, \beta_i)}{\partial \mathbb{T}}[\boldsymbol{\tau}] = \boldsymbol{\tau} \cdot \mathbb{B}_i^2[\boldsymbol{\tau}] = \mathbb{B}_i[\boldsymbol{\tau}] \cdot \mathbb{B}_i[\boldsymbol{\tau}] = ||\mathbb{B}_i[\boldsymbol{\tau}]||^2 \geq 0 \quad \text{for all} \quad \boldsymbol{\tau} \in \mathrm{Sym}(d). \tag{2.26}$$

In addition to the damage functions, we assume a hardening-type damage-surface potential of power-law type

$$h(q) = \sum_{i=1}^{M} \frac{G_i}{m_i + 1} q_i^{m_i+1}, \quad m_i > 0, \tag{2.27}$$

involving a positive, dimension-free power-law exponent m_i and a positive hardening parameter G_i with dimensions of stress. Thus, according to (2.22), the damage-driving forces compute as

$$\beta_i = -G_i q_i^{m_i}, \quad i = 1, \ldots, M. \tag{2.28}$$

In view of the force potential Φ^* (2.20) and the driving forces $\mathbb{T}$ (2.18) and β (2.28), there is an *elastic domain* in the (extended) stress space, described by the conditions

$$||\mathbb{B}_i[\boldsymbol{\sigma}]||^2 \leq \sigma_{0,i}^2 + G_i H_i q_i^{m_i}, \quad i = 1, \ldots, M, \tag{2.29}$$

where no damage occurs. As defined in equations (2.21), the evolutions of the compliance and the damage-surface variables are governed by

$$\dot{\mathbb{S}} = 2 \sum_{i=1}^{M} \dot{\mu}_i \mathbb{B}_i^2 \quad \text{and} \quad \dot{q}_i = \dot{\mu}_i H_i, \quad i = 1, \ldots, M, \tag{2.30}$$

in case of an active damage system at index i – otherwise, $\dot{\mu}_i = 0$ holds.

Several simplifications are in order. First, notice that the parameters G_i and H_i only enter (2.29) as the product $G_i H_i$. As we may redefine $\tilde{G}_i = \tilde{H}_i = \sqrt{G_i H_i}$ without changing the elastic domain (2.29), we assume $G_i = H_i$. Secondly, we may eliminate the consistency parameter from the evolution of the compliance (2.30) and integrate to get

$$\mathbb{S}(t) = \mathbb{S}_0 + 2\sum_{i=1}^{M} \frac{q_i(t)}{H_i} \mathbb{B}_i^2, \tag{2.31}$$

where $\mathbb{S}_0 = \mathbb{S}(0)$ is the initial compliance. Thirdly, in three spatial dimensions $d = 3$, the compliance tensor $\mathbb{S}$ is described by 21 independent parameters. The latter formula (2.31) permits us to express the current compliance tensor $\mathbb{S}$ in terms of the internal variables q. Thus, with an eye towards an efficient implementation, we may a posteriori *eliminate* the compliance tensor $\mathbb{S}$ from the model. Furthermore, as stated above, notice that the equations (2.30) permit us to eliminate the parameters $\dot{\mu}$ completely. Last but not least, in view of the elastic domain (2.29), we may work with the damage-activation functions f_i

$$f_i : \mathrm{Sym}(d) \times \mathbb{R} \to \mathbb{R}, \quad (\boldsymbol{\sigma}, q_i) \mapsto ||\mathbb{B}_i[\boldsymbol{\sigma}]||^2 - \sigma_{0,i}^2 - H_i^2 q_i^{m_i}, \quad i = 1, \ldots, M, \tag{2.32}$$

instead of the original functions ϕ_i (2.25). For the convenience of the reader, we summarize the key aspects of the model in the following box.

Summary of compliance-based convex damage model (primal formulation)

Input Initial compliance tensor $\mathbb{S}_0$, extraction tensors $\mathbb{B}_i$, hardening moduli $H_i > 0$, damage thresholds $\sigma_{0,i} > 0$, power-law exponents $m_i > 0$ $(i = 1, \ldots, M)$.

Evolution equations For given strain path $\boldsymbol{\varepsilon} : [0, T] \to \mathrm{Sym}(d)$, find damage-hardening variables $q : [0, T] \to \mathbb{R}^M$ and a stress path $\boldsymbol{\sigma} : [0, T] \to \mathrm{Sym}(d)$, s. t.

$$f_i(\boldsymbol{\sigma}, q_i) \leq 0, \quad \dot{q}_i \geq 0, \quad \dot{q}_i f_i(\boldsymbol{\sigma}, q_i) = 0, \quad i = 1, \ldots, M, \tag{2.33}$$

holds, with initial conditions $q(0) = 0$, and where

$$f_i(\boldsymbol{\sigma}, q_i) = ||\mathbb{B}_i[\boldsymbol{\sigma}]||^2 - \sigma_{0,i}^2 - H_i^2 q_i^{m_i} \quad \text{and} \quad \boldsymbol{\varepsilon} = \left(\mathbb{S}_0 + 2\sum_{i=1}^{M} \frac{q_i}{H_i} \mathbb{B}_i^2 \right)[\boldsymbol{\sigma}]. \tag{2.34}$$

Computational predictor-corrector framework

In this section, upon an implicit Euler discretization in time, we discuss a predictor-corrector solution strategy for the model introduced in the previous section in strict analogy to associative elastoplasticity, see Chapter 2 in Simo and Hughes (1998). Suppose that a number of discrete time steps $0 = t_0 < t_1 < \ldots < t_{N-1} < t_N = T$ is given, together with prescribed strain tensors $\boldsymbol{\varepsilon}_0, \boldsymbol{\varepsilon}_1, \ldots \boldsymbol{\varepsilon}_N$, an initial compliance tensor $\mathbb{S}_0$ and the initial damage-hardening variable $q_0 \equiv 0 \in \mathbb{R}^M$. For any $n = 0, \ldots, N-1$, dropping the subscript $n+1$ for simplicity of notation, we seek $(\boldsymbol{\sigma}, q) \in \mathrm{Sym}(d) \times \mathbb{R}^M$ solving the system of equations

$$\begin{aligned} \boldsymbol{\varepsilon} &= \left(\mathbb{S}_0 + 2\sum_{i=1}^{M} \frac{q_i}{H_i}\mathbb{B}_i^2\right)[\boldsymbol{\sigma}] \\ f_i(\boldsymbol{\sigma}, q_i) &\leq 0, \quad q_i - q_{i,n} \geq 0, \quad (q_i - q_{i,n}) f_i(\boldsymbol{\sigma}, q_i) = 0, \quad i = 1, \ldots, M, \end{aligned} \tag{2.35}$$

with the damage functions f_i $(2.34)_1$. With a computational resolution in mind, we rewrite the system (2.35) in terms of active sets. For any $(\boldsymbol{\sigma}, q) \in \mathrm{Sym}(d) \times \mathbb{R}^M$, the *active set* $\mathcal{A}(\boldsymbol{\sigma}, q)$ is defined as

$$\mathcal{A}(\boldsymbol{\sigma}, q) = \left\{ i \in \{1, 2, \ldots, M\} \,|\, f_i(\boldsymbol{\sigma}, q_i) \geq 0 \right\}, \tag{2.36}$$

collecting all indices of inequality constraints that are either violated or satisfied exactly. Then, as a consequence of the complementarity condition in the system (2.35), $(\boldsymbol{\sigma}, q) \in \mathrm{Sym}(d) \times \mathbb{R}^M$ solves the system (2.35) precisely if it satisfies $q_i \geq q_{i,n}$ $(i = 1, \ldots, M)$ and solves

$$\begin{aligned} \left(\mathbb{S}_0 + 2\sum_{i=1}^{M} \frac{q_i}{H_i}\mathbb{B}_i^2\right)[\boldsymbol{\sigma}] &= \boldsymbol{\varepsilon} \\ f_i(\boldsymbol{\sigma}, q_i) &= 0 \quad \text{for all} \quad i \in \mathcal{A}(\boldsymbol{\sigma}, q). \end{aligned} \tag{2.37}$$

We solve the latter problem by an active set strategy (Bergounioux et al., 1999, 2000), i.e., by solving the system (2.37) with a Newton method, updating the currently active set at each Newton iteration and accounting for the constraints $q_i \geq q_{i,n}$ $(i = 1, \ldots, M)$ via backtracking. The details comprise Alg. 1, where $\gamma \in (0, 1)$ is a backtracking factor. We use a backtracking factor of $\gamma = 0.9$ in our presented examples.

As long as the damage constraints are linearly independent, due to the established connections of active set strategies to semi-smooth Newton methods, see Hintermüller et al. (2002), a locally superlinear convergence behavior can be expected. A schematic of the predictor-corrector strategy is shown in Figure 3 with

$$\text{residual}(\boldsymbol{\sigma}, q) = \frac{\sqrt{\|\boldsymbol{\sigma} - \left(\mathbb{S}_0 + 2\sum_{i=1}^{M} q_i \mathbb{B}_i^2 / H_i\right)^{-1}[\boldsymbol{\varepsilon}]\|^2 + \sum_{i=1}^{M} \max\{0, f_i(\boldsymbol{\sigma}, q_i)\}}}{||\boldsymbol{\sigma}||} \tag{2.38}$$

for measuring convergence. Whenever the trial stress fails to be contained in the elastic region, an iterative process is initiated which ensures that the final stress state again lies on the boundary of the elastic domain. For the latter, both the elastic region may grow – as a result of the damage-hardening – and the stress may decrease – owing to increasing compliance.

For solving problem (2.37), we assemble the Newton system for the active set $\mathcal{A}(\boldsymbol{\sigma}, q)$

$$\begin{aligned} \left(\mathbb{S}_0 + 2\sum_{i=1}^{M} \frac{q_i}{H_i}\mathbb{B}_i^2\right)[\triangle\boldsymbol{\sigma}] + \sum_{i=1}^{M} \frac{2}{H_i}\mathbb{B}_i^2[\boldsymbol{\sigma}]\, \triangle q_i &= \boldsymbol{\varepsilon} - \left(\mathbb{S}_0 + 2\sum_{i=1}^{M} \frac{q_i}{H_i}\mathbb{B}_i^2\right)[\boldsymbol{\sigma}] \\ \left(\frac{2}{H_i}\,\mathbb{B}_i^2[\boldsymbol{\sigma}]\right) \cdot \triangle\boldsymbol{\sigma} - m_i H_i q_i^{m_i - 1} \triangle q_i &= -\frac{1}{H_i}\left(||\mathbb{B}_i[\boldsymbol{\sigma}]||^2 - \sigma_{0,i}^2 - H_i^2 q_i^{m_i}\right) \end{aligned} \tag{2.39}$$

for all $i \in \mathcal{A}(\boldsymbol{\sigma}, q)$, where we divided the second line by H_i to ensure a symmetric Newton system.

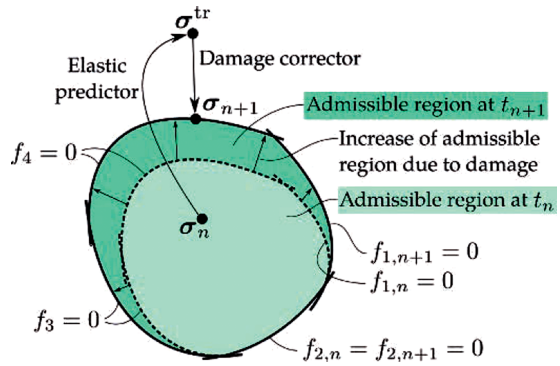

Figure 3. Evolution of the elastic region upon loading within a predictor-corrector framework.

Algorithm 1 Predictor-corrector strategy $(\varepsilon, q_{i,n})$ with model parameters $(\mathbb{S}_0, \mathbb{B}_i, H_i, \sigma_{0,i}, m_i)$ and algorithm parameters $(\text{maxit}, \text{tol}, \gamma)$

Elastic predictor
$q \leftarrow q_n$
$\boldsymbol{\sigma} \leftarrow \left(\mathbb{S}_0 + 2\sum_{i=1}^{M} q_i \, \mathbb{B}_i^2 / H_i \right) [\varepsilon]$
if all $f_i \leq 0$ **then**
  no damage evolution, elastic predictor step correct
else
  Damage corrector
  $k \leftarrow 1$ ▷ Iteration counter
  Update residual (2.38)
  while $k <$ maxit **and** residual $>$ tol **do**
    $\mathcal{A} \leftarrow \mathcal{A}(\boldsymbol{\sigma}, q)$
    assemble and solve the Newton system (2.39) for $(\triangle\boldsymbol{\sigma}, \triangle q)$ ▷ $\triangle q_i := 0$ for $i \neq \mathcal{A}$
    $s \leftarrow 1$ ▷Full step size
    $(\boldsymbol{\sigma}, q) \leftarrow (\boldsymbol{\sigma} + s\,\triangle\boldsymbol{\sigma}, q + s\,\Delta q)$
    $j \leftarrow 0$ ▷ Counts backtracking steps
    $\text{residual}_{\text{old}} \leftarrow$ residual
    Update residual (2.38)
    while residual $>$ $\text{residual}_{\text{old}}$ **or** $q_i < q_{i,n}$ for some i **do** ▷ Backtracking, typically $\gamma = 0.9$
      $(\boldsymbol{\sigma}, q) \leftarrow (\boldsymbol{\sigma} + (\gamma s - s)\triangle\boldsymbol{\sigma}, q + (\gamma s - s)\triangle q)$
      $s \leftarrow \gamma s$ ▷ Reduce current step size
      Update residual (2.38)
      $j \leftarrow j + 1$
    end while
    $k \leftarrow k + 1$
  end while
end if
compute $\mathbb{C}_{\text{algo}}$
Output
return $\boldsymbol{\sigma}$, q, $\mathbb{C}_{\text{algo}}$

Damage models with Puck-type extraction tensors

Basic idea

Puck (Knops, 2008; Puck and Schürmann, 2002) introduced strength-estimation models for composites reinforced by continuous fibers based on specfic failure scenarios that are commonly observed in post-critical investigations of failed specimens. For the current article at hand, we will use these so-called Puck cases as primary drivers of the anisotropic damage evolution presented in the previous section. More precisely, we will investigate the Puck cases individually, and determine proper extraction tensors ($\mathbb{B}_{\mathrm{I}}$ - $\mathbb{B}_{\mathrm{IV}}$). These Puck-type extraction tensors are motivated by the stress and corresponding damage states present in the fiber bundle mesostructure of Sheet Molding Compound (SMC) composites (Dumont et al., 2007; Görthofer et al., 2019).

We introduce a local Cartesian coordinate system $\{\boldsymbol{e}_1, \boldsymbol{e}_2, \boldsymbol{e}_3\}$, s. t. the fibers are aligned to the $\boldsymbol{e}_1$-direction, see Figure 4(a). Then, the stress state $\boldsymbol{\sigma}$ may be decomposed into blocks

$$\boldsymbol{\sigma} = \left(\begin{array}{c|cc} \sigma_{11} & \sigma_{12} & \sigma_{13} \\ \hline \sigma_{12} & \sigma_{22} & \sigma_{23} \\ \sigma_{13} & \sigma_{23} & \sigma_{33} \end{array}\right), \tag{3.1}$$

where σ_{11} is the stress in fiber direction, the lower right block describes the stresses in the plane orthogonal to the fiber direction, and $(\sigma_{12}, \sigma_{13})$ collects the remaining shear stresses. Adopting ideas of Puck (Knops, 2008; Puck and Schürmann, 2002), we distinguish four basic cases which drive the damage evolution in a fiber bundle, for instance.

(I)	Normal loading in fiber direction	σ_{11}	▷ Figure 4(a) and (b)
(II)	Normal loading perpendicular to fiber direction	σ_{22}, σ_{33}	▷ Figure 4(c) and (d)
(III)	Shear loading perpendicular to fiber direction	σ_{23}	▷ Figure 4(e)
(IV)	Shear loading in fiber direction	σ_{12}, σ_{13}	▷ Figure 4(f)

The loading scenarios shown in Figure 4 are only examples, e.g., loadings perpendicular to the fiber direction need not necessarily follow direction $\boldsymbol{e}_2$. Instead, any other direction in the $\boldsymbol{e}_2$-$\boldsymbol{e}_3$-plane could be used, as well. Nevertheless, we may regard a general loading scenario as a superposition of the four introduced cases. In the following sections, we will derive appropriate extraction tensors ($\mathbb{B}_{\mathrm{I}}$ - $\mathbb{B}_{\mathrm{IV}}$) corresponding to each of the four presented cases based on averaged stress conditions. The presented model cannot distinguish between tensile and compressive loading, as the driving force $\mathbb{T}$ (2.18) is quadratic in the stress $\boldsymbol{\sigma}$. Consequently, the six sketched loading scenarios in Figure 4 reduce to the mentioned four cases, as the scenarios Figure 4(a) and (b), as well as Figure 4(c) and (d) coincide for our model.

Case I: Normal loading in fiber direction

The first damage case is governed by loading in fiber or bundle direction, respectively, and thus solely concerns the stress σ_{11}. For fiber direction $\boldsymbol{e}_1$, the fourth-order extraction tensor $\mathbb{B}_{\mathrm{I}}$ extracting

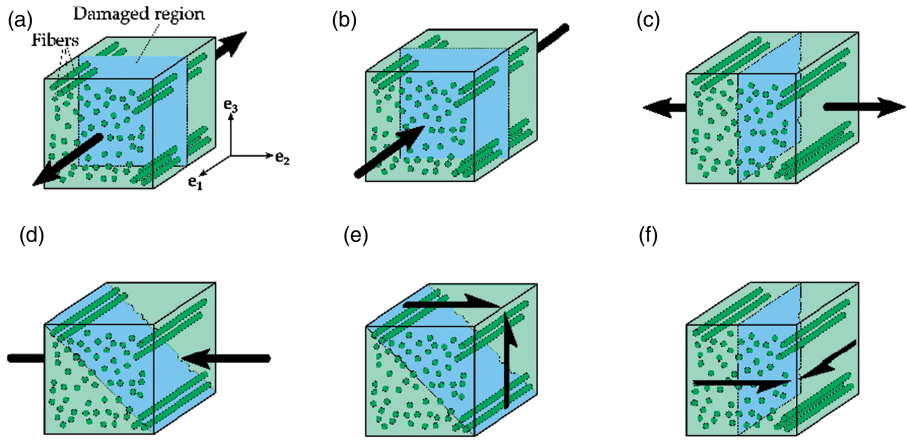

Figure 4. Regions of major damage (blue) resulting from different loading scenarios in a cell with aligned fibers (dark green). (a) Extension in fiber direction. (b) Compression in fiber direction. (c) Extension $\perp$ to fiber direction. (d) Compression $\perp$ to fiber direction. (e) Shearing $\perp$ to fiber direction. (f) Shearing in fiber direction.

the stress in bundle direction σ_{11} from an arbitrary stress state $\boldsymbol{\sigma}$ is given by

$$\mathbb{B}_{\mathrm{I}} = \boldsymbol{e}_1^{\otimes 4}. \tag{3.2}$$

The associated damage function $(2.34)_1$ with case I extraction tensor $\mathbb{B}_{\mathrm{I}}$ (3.2) reads

$$f_{\mathrm{I}}(\boldsymbol{\sigma}, q) = \sigma_{11}^2 - H^2 q^m - \sigma_0^2, \tag{3.3}$$

and will solely induce a decrease in the Young's modulus in $\boldsymbol{e}_1$-direction. As a general note, although the damage parameters like σ_0, H, m may differ for the considered cases I to IV, we do not include additional subscripts for the sake of readability.

Case II: Normal loading perpendicular to fiber direction

To quantify damaging due to normal loading in any direction $S^2 \ni \boldsymbol{n} \perp \boldsymbol{e}_1$ perpendicular to the fiber direction (a unit vector with $S^2 = \{\boldsymbol{x} \in \mathbb{R}^3 \,|\, ||\boldsymbol{x}|| = 1\}$), for a general stress state $\boldsymbol{\sigma}$, we measure the average normal stress perpendicular to the fiber direction

$$\frac{1}{2\pi}\int_0^{2\pi} \boldsymbol{n}(\theta)^{\otimes 4}[\boldsymbol{\sigma}]\,\mathrm{d}\theta \quad \text{with} \quad \boldsymbol{n}(\theta) \mathrel{\hat{=}} (0, \cos\theta, \sin\theta). \tag{3.4}$$

The latter average may be represented in the form

$$\frac{1}{2\pi}\int_0^{2\pi} \boldsymbol{n}(\theta)^{\otimes 4}[\boldsymbol{\sigma}]\,\mathrm{d}\theta \overset{!}{=} \mathbb{B}_{\mathrm{II}}[\boldsymbol{\sigma}] \tag{3.5}$$

in terms of the extraction tensor $\mathbb{B}_{\mathrm{II}}$

$$\mathbb{B}_{\mathrm{II}} = \frac{1}{2\pi}\int_0^{2\pi} \boldsymbol{n}(\theta)^{\otimes 4}\,\mathrm{d}\theta \quad \text{with} \quad \boldsymbol{n}(\theta) \hat{=} (0, \cos\theta, \sin\theta). \tag{3.6}$$

Evaluating the integral explicitly, see Appendix C for details, yields

$$\mathbb{B}_{\mathrm{II}} = \frac{1}{4}(\boldsymbol{e}_2^{\otimes 2} + \boldsymbol{e}_3^{\otimes 2})^{\otimes 2} + \frac{1}{8}(\boldsymbol{e}_2^{\otimes 2} - \boldsymbol{e}_3^{\otimes 2})^{\otimes 2} + \frac{1}{2}(\boldsymbol{e}_2 \otimes_{\mathrm{S}} \boldsymbol{e}_3)^{\otimes 2}. \tag{3.7}$$

This extraction tensor $\mathbb{B}_{\mathrm{II}}$ is identical to the fourth-order fiber-orientation tensor for a planar isotropic orientation, see Advani and Tucker (1987). The damage function $(2.34)_1$ involving the case II extraction tensor $\mathbb{B}_{\mathrm{II}}$ (3.7) reads

$$f_{\mathrm{II}}(\boldsymbol{\sigma}, q) = \frac{1}{32}\left(5\sigma_{22}^2 + 5\sigma_{33}^2 + 6\sigma_{22}\sigma_{33} + 4\sigma_{23}^2\right) - H^2 q^m - \sigma_0^2. \tag{3.8}$$

Case III: Shear loading perpendicular to fiber direction

In addition to damage caused by normal loading, we also want to account for shear-loading induced damage. For a general stress state $\boldsymbol{\sigma}$, the average shear stress transverse to the fiber direction is given by

$$\frac{1}{2\pi}\int_0^{2\pi} (\boldsymbol{n}(\theta) \otimes_{\mathrm{S}} \boldsymbol{m}(\theta))^{\otimes 2}[\boldsymbol{\sigma}]\,\mathrm{d}\theta \tag{3.9}$$

$$\text{with} \quad \boldsymbol{n}(\theta) \hat{=} (0, \cos\theta, \sin\theta) \quad \text{and} \quad \boldsymbol{m}(\theta) \hat{=} (0, -\sin\theta, \cos\theta).$$

We may rewrite this expression

$$\frac{1}{2\pi}\int_0^{2\pi} (\boldsymbol{n}(\theta) \otimes_{\mathrm{S}} \boldsymbol{m}(\theta))^{\otimes 2}[\boldsymbol{\sigma}]\,\mathrm{d}\theta ! \mathbb{B}_{\mathrm{III}}[\boldsymbol{\sigma}] \tag{3.10}$$

in terms of the extraction tensor $\mathbb{B}_{\mathrm{III}}$ as

$$\mathbb{B}_{\mathrm{III}} = \frac{1}{2\pi}\int_0^{2\pi} (\boldsymbol{n}(\theta) \otimes_{\mathrm{S}} \boldsymbol{m}(\theta))^{\otimes 2}\,\mathrm{d}\theta \tag{3.11}$$

$$\text{with} \quad \boldsymbol{n}(\theta) \hat{=} (0, \cos\theta, \sin\theta) \quad \text{and} \quad \boldsymbol{m}(\theta) \hat{=} (0, -\sin\theta, \cos\theta).$$

Explicitly evaluating the integral (3.11) yields

$$\mathbb{B}_{\mathrm{III}} = \frac{1}{8}\left(\boldsymbol{e}_2^{\otimes 2} - \boldsymbol{e}_3^{\otimes 2}\right)^{\otimes 2} + \frac{1}{2}(\boldsymbol{e}_2 \otimes_{\mathrm{S}} \boldsymbol{e}_3)^{\otimes 2}. \tag{3.12}$$

The damage function $(2.34)_1$ for the case III extraction tensor $\mathbb{B}_{\mathrm{III}}$ (3.12) reads

$$f_{\mathrm{III}}(\boldsymbol{\sigma}, q) = \frac{1}{32}\left(\sigma_{22}^2 + \sigma_{33}^2 - 2\sigma_{22}\sigma_{33} + 4\sigma_{23}^2\right) - H^2 q^m - \sigma_0^2. \tag{3.13}$$

Comparing the extraction tensors $\mathbb{B}_{\mathrm{II}}$ (3.7) and $\mathbb{B}_{\mathrm{III}}$ (3.12), some similarities between these tensors become apparent. In fact, these similarities reflect the relationship between normal loadings (especially compression) and shear loadings perpendicular to the fiber direction, that are familiar from undergraduate engineering mechanics (Hibbeler, 2001), i.e., Mohr's circle (Mohr, 1900).

Case IV: Shear loading in fiber direction

To evaluate damage induced by shearing in fiber direction $\boldsymbol{e}_1$, we evaluate

$$\frac{1}{2\pi}\int_0^{2\pi} \left(\boldsymbol{n}(\theta)\otimes_{\mathrm{S}}\boldsymbol{e}_1\right)^{\otimes 2}[\boldsymbol{\sigma}]\,\mathrm{d}\theta \quad \text{with} \quad \boldsymbol{n}(\theta) \mathrel{\hat{=}} (0, \cos\theta, \sin\theta), \tag{3.14}$$

which we represent in the form

$$\frac{1}{2\pi}\int_0^{2\pi} \left(\boldsymbol{n}(\theta)\otimes_{\mathrm{S}}\boldsymbol{e}_1\right)^{\otimes 2}[\boldsymbol{\sigma}]\,\mathrm{d}\theta \overset{!}{=} \mathbb{B}_{\mathrm{IV}}[\boldsymbol{\sigma}] \tag{3.15}$$

with extraction tensor $\mathbb{B}_{\mathrm{IV}}$

$$\mathbb{B}_{\mathrm{IV}} = \frac{1}{2\pi}\int_0^{2\pi} \left(\boldsymbol{n}(\theta)\otimes_{\mathrm{S}}\boldsymbol{e}_1\right)^{\otimes 2}\mathrm{d}\theta \quad \text{and} \quad \boldsymbol{n}(\theta) \mathrel{\hat{=}} (0, \cos\theta, \sin\theta). \tag{3.16}$$

The resulting extraction tensor for case IV may be expressed via

$$\mathbb{B}_{\mathrm{IV}} = \frac{1}{2}\left(\boldsymbol{e}_1\otimes_{\mathrm{S}}\boldsymbol{e}_2\right)^{\otimes 2} + \frac{1}{2}\left(\boldsymbol{e}_1\otimes_{\mathrm{S}}\boldsymbol{e}_3\right)^{\otimes 2}. \tag{3.17}$$

The damage function $(2.34)_1$ with case IV extraction tensor $\mathbb{B}_{\mathrm{IV}}$ (3.17) becomes

$$f_{\mathrm{IV}}(\boldsymbol{\sigma}, q) = \frac{1}{8}\left(\sigma_{12}^2 + \sigma_{13}^2\right) - H^2 q^m - \sigma_0^2. \tag{3.18}$$

Computational investigations

Setup

We integrated the proposed damage model as a user-defined subroutine into an in-house OpenMP-parallel FFT-based computational homogenization code written in Python 3.7 with Cython extensions (Behnel et al., 2011) and FFTW (Frigo and Johnson, 2005) bindings, as described, e.g., by Schneider (2019). The balance of linear momentum was discretized on a staggered grid (Schneider et al., 2016b) and the ensuing nonlinear systems of equations were solved by a Newton-CG scheme

Table 1. Standard material parameters (Kehrer et al., 2018) and reference damage parameters, serving as point of departure depending on the corresponding damage case.

UPPH matrix	E-glass fibers	Damage parameters
$E_M = 3.4$ GPa	$E_F = 72$ GPa	$\sigma_0 \in [5, 30]$ MPa, $m = 1$
$\nu_M = 0.385$	$\nu_F = 0.22$	$H \in [30, 80]$ MPa

(Gélébart and Mondon-Cancel, 2013; Kabel et al., 2014; Wicht et al., 2020). The computations ran on 6 - 12 threads on a desktop computer with 32 GB RAM and an Intel i7-8700K CPU with 6 cores and a clock rate of 3.7 GHz. The plain-weave presented at the end of this section was computed on a workstation with two AMD EPYC 7642 and 48 physical cores each, enabled SMT, and 1024 GB of DRAM.

For the following studies, we use the isotropic elastic parameters of unsaturated polyester-polyurethane hybrid (UPPH) resin and E-glass fibers, see Kehrer et al. (2018), respectively, if not specified otherwise. Furthermore, we use the damage parameters σ_0, H and m listed in Table 1 as a point of departure for parameter variation and the different introduced damage cases. Due to the small-strain setting, we limit the strain axes to 5 % in magnitude.

Numerical studies on integration-point level

Parameter study for Puck-type extraction tensor I. The first study concerns the effects of the damage parameters σ_0, H and m on the stress and damage evolution. For this purpose, we investigate the model behavior for one active damage function and the Puck-type extraction tensor I only. We vary the parameters and evaluate the stress-strain curves, as well as the normalized Young's modulus E_{11}/E_{11}^0 for uniaxial extension in $\boldsymbol{e}_1$-direction and a prescribed strain ε_{11}.

For the case at hand, we extract the current Young's modulus in $\boldsymbol{e}_1$-direction from equation (2.31) by

$$E_{11} = HE_{11}^0/(H + 2\,q\,E_{11}^0), \tag{4.1}$$

where E_{11}^0 stands for the initial Young's modulus in $\boldsymbol{e}_1$-direction. Please note that E_{11}^{-1} may be regarded as a component of a (fourth-order) tensor, as it is the 1111 component of the corresponding compliance $\mathbb{S}$. For the sake of simplicity, we will use such shorthand index notation for certain Young's moduli throughout the remainder of this work.

The influence of the damage-activation threshold σ_0 on the stress and normalized stiffness in $\boldsymbol{e}_1$-direction is shown in Figure 5. The higher the damage-activation threshold σ_0, the later the damage evolution initiates w. r. t. the applied strain ε_{11}. In Figure 5(a), we observe damage to initiate as soon as the stress σ_{11} equals the damage-activation threshold σ_0, which is expected. The convex hardening nature of our model gives rise to a decreasing slope of the stress-strain curve. This slope tends to zero at infinity, but remains non-negative.

With increasing damage-activation thresholds σ_0, the stress-strain behavior approaches a plateau beyond the elastic region, in which an increase of strain does not induce a further increase of stress. The reduced stiffness E_{11} in $\boldsymbol{e}_1$-direction equals the slope of the stress-strain curve during unloading (which returns to the origin in our pure elastic-damage framework). Whereas the plateaus are more pronounced for higher damage-activation thresholds σ_0, the increase in damage and the (normalized) stiffness reduction are less pronounced, see Figure 5(b).

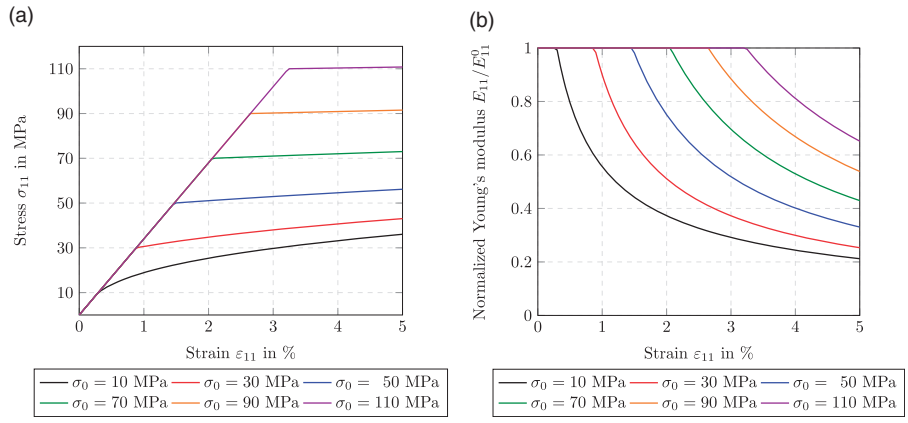

Figure 5. Varying the initial stress σ_0 for the proposed model. (a) Stress-strain curve. (b) Normalized Young's modulus vs. applied strain.

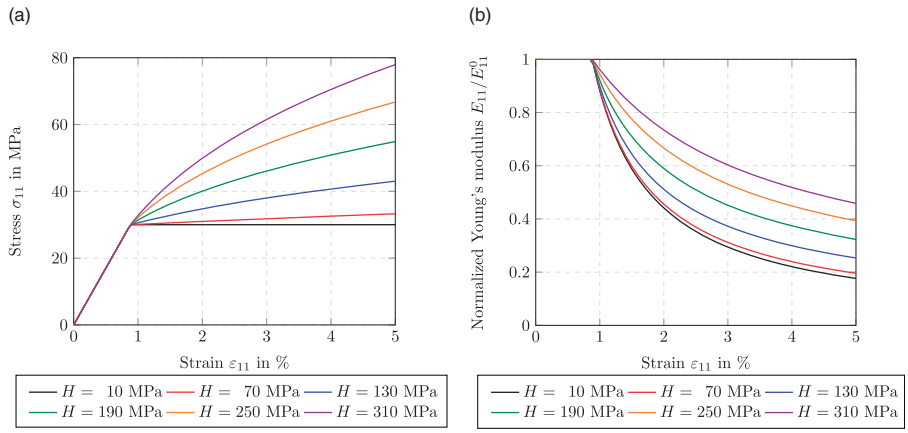

Figure 6. Varying the hardening parameter H for the proposed model. (a) Stress-strain curve. (b) Normalized Young's modulus vs. applied strain.

Due to the thermodynamically consistent GSM framework of our proposed model, an upper bound for the damage variables is ensured, governing the asymptotic behavior of the (normalized) stiffness reduction, see Figure 5(b). Evaluating the CDI (2.2) for the considered case at hand, we find the upper bound for the damage variable w. r. t. Puck case I to be $q_{\mathrm{I}} \leq \sqrt[m]{\sigma_{11}^2/H^2}$.

The effect of changing the hardening parameter H on the stress and damage evolution is shown in Figure 6. As the damage-activation threshold σ_0 remains unchanged for this study, the elastic regions (σ_{11} below 30 MPa) coincide for all stress-strain curves, see Figure 6(a).

In the damage region, the slope of the stress-strain curve increases with the hardening parameter H. Indeed, the hardening parameter H describes the hardening capacity of the model. For $H \to 0$, the slope tends to zero and approaches the plateau already observed in Figure 5(a). For $H \to \infty$, an active

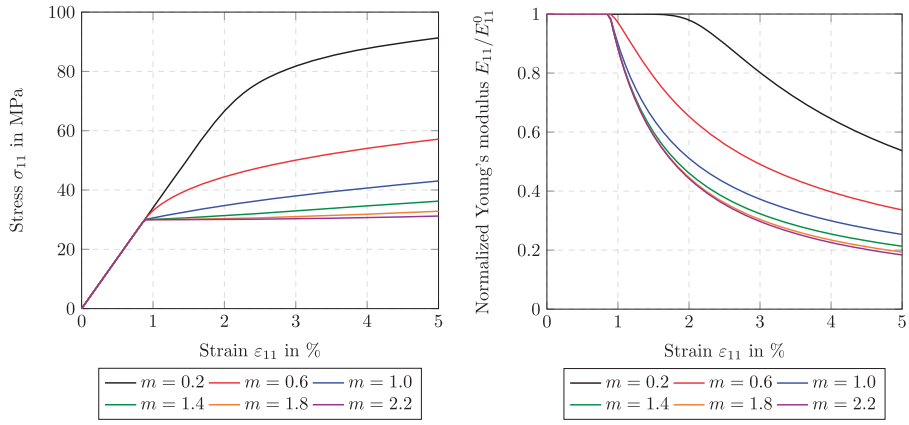

Figure 7. Varying the power-law exponent m for the proposed model. (a) Stress-strain curve. (b) Normalized Young's modulus vs. applied strain.

damage function $f\,(2.34)_1$ will become inactive for small values of the damage variable $q \to 0$, resulting in a damage region that can hardly be distinguished from a purely elastic material behavior.

Independent of the hardening parameter, damage evolution initiates at the same strain level (and therefore the same stress level), see Figure 6(b). The stiffness reduction is inversely proportional to the hardening parameter H.

In Figure 7, we fix the damage-activation threshold σ_0 as well as the hardening parameter H and vary the power-law exponent m. In contrast to the influence of the hardening parameter H (see Figure 6), the slope of the stress-strain curve is inversely proportional to the exponent m in the damage region, see Figure 7(a).

For increasing exponents m, the stress-strain curves approach the plateau-like behavior. For small values of m, after exceeding the damage-activation threshold σ_0, the stress-strain curves remain approximately linear and only develop a significant amount of damage for higher loading levels.

Figure 7(b) shows the damage evolution to be inversely proportional to the exponent m, leading to a lower remaining (normalized) stiffness component E_{11} for higher exponents m.

For representing the stiffness tensor $\mathbb{C} = \mathbb{S}^{-1}$ graphically, we use the Young's modulus surface (YMS) plots introduced by Böhlke and Brüggemann (2001), i.e., for fixed compliance tensor $\mathbb{S} \in \mathcal{S}_d$, the image of the nonlinear mapping

$$S^2 \to \mathbb{R}^3, \quad \boldsymbol{n} \mapsto E(\mathbb{S}, \boldsymbol{n})\,\boldsymbol{n}, \tag{4.2}$$

where the Young's modulus $E(\mathbb{S}, \boldsymbol{n})$ in direction $\boldsymbol{n}$ is determined by

$$E(\mathbb{S}, \boldsymbol{n}) = \frac{1}{(\boldsymbol{n} \otimes \boldsymbol{n}) \cdot \mathbb{S}[\boldsymbol{n} \otimes \boldsymbol{n}]}. \tag{4.3}$$

Asymmetry properties of the stiffness tensor $\mathbb{C}$ become apparent in the corresponding YMS plot.

Examples of such YMS plots are shown in Figure 8. The initially isotropic stiffness tensor with UPPH material parameters (see Table 1) has a spherical shape, as shown in Figure 8(a). As

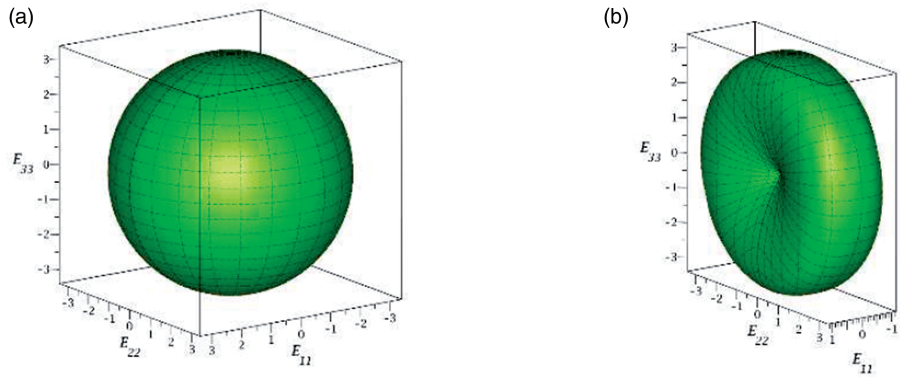

Figure 8. YMS plots (see Böhlke and Brüggemann, 2001) showing the reduction of the stiffness tensor based on Puck case I. (a) Initial isotropic state. (b) Final anisotropic state.

discussed above, the induced damage model based on Puck case I leads to a reduction of the stiffness E_{11} in the $\boldsymbol{e}_1$-direction. The YMS plot is contracted in the direction of loading, whereas the directional Young's moduli in the orthogonal plane remain unaffected, see Figure 8(b).

Stiffness reduction for different Puck-type extraction tensors. In the following, we will discuss possible damage evolutions and corresponding stiffness reductions based on Puck-type extraction tensors II, III and IV. For these cases, the influence of the damage-hardening parameters σ_0, H and m is similar to case I, which we discussed in the previous section. We consider an initially isotropic stiffness tensor with UPPH material parameters. The corresponding YMS plot is shown in Figure 8(a). Specific loadings will evoke a damage evolution due to the Puck cases II, III and IV. We apply a normal strain ε_{22} for case II, a shear strain ε_{23} for case III and a shear strain ε_{13} for case IV, forcing the respective complementary stress components to zero. The resulting YMS plots are shown in Figure 9. For all three cases the Young's modulus in $\boldsymbol{e}_1$-direction remains unchanged. As shortly discussed in the previous chapter, Puck cases II and III are interlinked due to similar effects of averaged normal loadings and shear loadings perpendicular to the fiber direction. Inspecting Figure 9(a) and (b), corresponding to Puck cases II and III, we observe a reduction of the Young's moduli within the $\boldsymbol{e}_2$-$\boldsymbol{e}_3$-plane for both cases, but with different characteristics. For the loading scenarios considered here, the stiffness reduction in directions $\boldsymbol{e}_2$ and $\boldsymbol{e}_3$ is more pronounced for Puck case II compared to Puck case III. Figure 9(c) shows that damage based on Puck case IV does not affect the Young's moduli in the $\boldsymbol{e}_2$-$\boldsymbol{e}_3$-plane. Young's moduli in the $\boldsymbol{e}_1$-$\boldsymbol{e}_3$-plane and $\boldsymbol{e}_1$-$\boldsymbol{e}_2$-plane are reduced equally, leading to a transversely isotropic stiffness with the fiber direction $\boldsymbol{e}_1$ as the axis of symmetry.

Non-monotonic loading. To show the capabilities of our model in general, we perform loading-unloading experiments for different loading directions in a successive fashion. To mimic uniaxial normal loadings and corresponding shear loadings, we subsequently apply normal and shear strains ε_{11}, ε_{22}, ε_{33}, ε_{23}, ε_{13} and ε_{12}, each with mixed boundary conditions permitting solely the corresponding stresses σ_{11}, σ_{22}, σ_{33}, σ_{23}, σ_{13} and σ_{12}, to be non-zero, see Figure 10(a) and (b). Lateral contraction is permitted. Between each of these six loading steps we unload to zero strain and stress. The resulting evolution of the stress components is plotted in Figure 10(b). We see a linear elastic region for each individual loading step and a damage region for all but the σ_{33} and σ_{12} cases. On

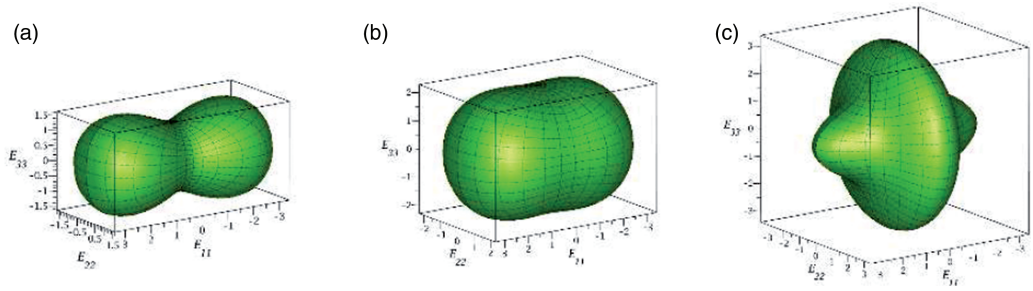

Figure 9. YMS plots (see Böhlke and Brüggemann, 2001) illustrating the reduction of the stiffness tensor based on the Puck cases II, III and IV. (a) Case II. (b) Case III. (c) Case IV.

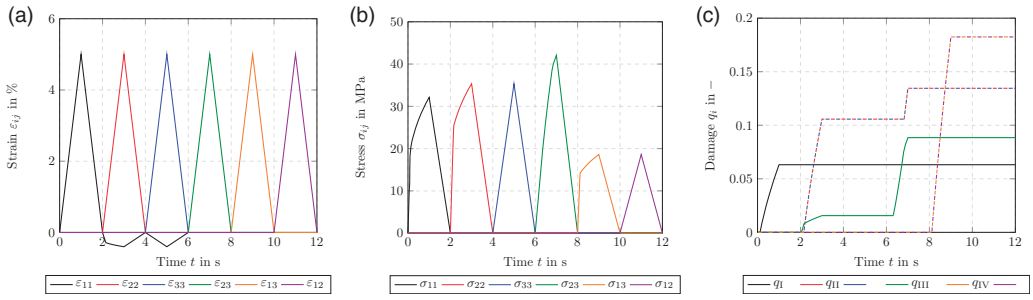

Figure 10. Complex loading history addressing each stress-tensor component separately. (a) Strain vs. time. (b) Stress vs. time. (c) Damage evolution over time.

these occasions, the threshold for damage initiation is not triggered. As all normal loadings in the $\boldsymbol{e}_2$-$\boldsymbol{e}_3$-plane evoke damage due to case II, σ_{33} cannot induce damage beyond the level previously induced. The stress-strain curves for the shear stresses σ_{13} and σ_{12} exhibit a similar behavior.

These observations are also reflected in the damage evolution, see Figure 10(c). Due to the applied stress σ_{22}, the damage variable representing case II increases. For increasing stress σ_{33}, the damage variables remain unaffected up to the level $\sigma_{33} = \sigma_{22}$. The same line of argument applies to σ_{13} and σ_{12}. Again, we observe the connection between Puck cases II and III, i. e., each of the damage variables increases whenever a loading scenario is applied which progresses the other case. The damaged stiffness tensors corresponding to each loading step are visualized via their YMS plots in Figure 11. The different colors of the plots represent the different loading steps shown in Figure 10. Note that the ranges of the axes are adjusted accordingly and therefore vary from plot to plot as the damage increases from step to step.

Comparing Figure 11(b) and (c), as well as Figure 11(e) and (f), we see that, in accordance with Figure 10(c), no further damage is induced between these loading steps. The presented YMS plots demonstrate the capability of our model to evolve the stiffness tensor in a complex and anisotropic way. The model is capable of handling *any* initial stiffness, not restricted by a specific symmetry class, i.e., transversely isotropic or orthotropic. Furthermore, the stiffness tensor may also develop anisotropy - within the permissible set $\mathcal{S}_d$ (2.8) - as a result of a damaging process, owing to the introduced damage functions.

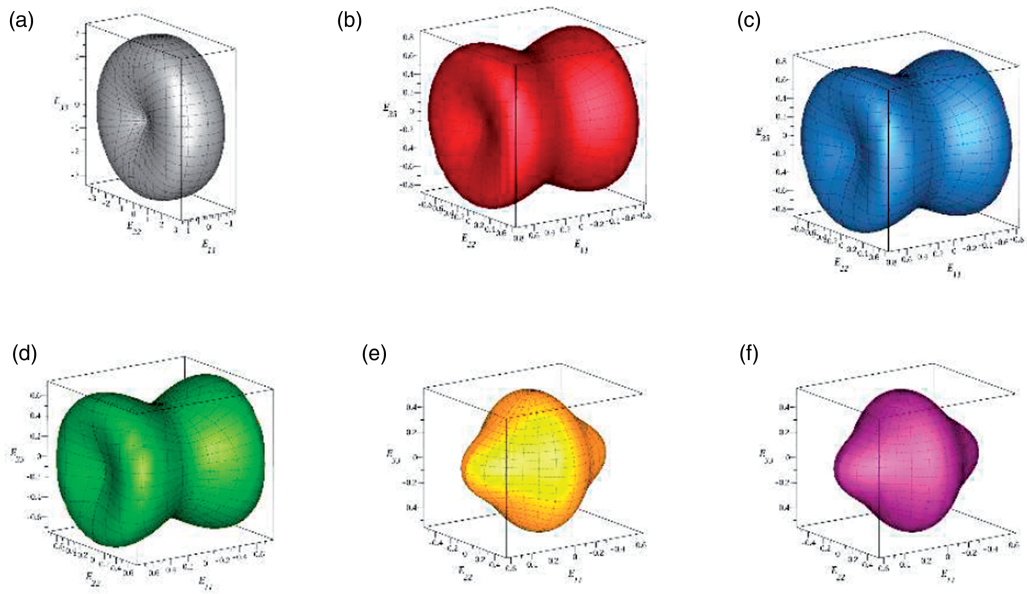

Figure 11. Evolution of an initially isotropic stiffness upon complex loading, see Figure 10(a), visualized via YMS plots. (a) After loading step 1 (ε_{11}). (b) After loading step 2 (ε_{11} and ε_{22}). (c) After loading step 3 (ε_{11}, ε_{22} and ε_{33}). (d) After loading step 4 (ε_{11}, ε_{22}, ε_{33} and ε_{23}). (e) After loading step 5 (ε_{11}, ε_{22}, ε_{33}, ε_{23} and ε_{13}). (f) After loading step 6 (ε_{11}, ε_{22}, ε_{33}, ε_{23}, ε_{13} and ε_{12}).

Multiaxial loading with increasing loading level. In a study combining the six loading steps from the previous section to one superposed loading case, we apply a three-dimensional strain state s. t. all strains are active simultaneously. To investigate the model behavior, the predicted stiffness degradation, as well as the evolution of the damage variables more closely, we gradually increase the strain levels in five steps from 0% to 5% via 1% increments with intermediate unloading, see Figure 12(a). As in the previous section, we analyze the stress and the damage evolution, as well as the stiffness reduction. Figure 12(b) shows the evolution of the individual stress components during the combined loading. We see that after each loading-unloading step the level of damage increases. This is also reflected in the evolution of the damage variables, see Figure 12(c). After each loading-unloading step, the damage variables continue to increase whenever the maximum stresses of the previous step are exceeded. The YMS plots corresponding to 2 % and 5 % loading, as well as the initially isotropic YMS plot, are shown in Figure 13. The stiffness tensor gradually reduces based on all four introduced Puck cases simultaneously. Apparently, the multiaxial loading evokes a stiffness reduction in all directions, as we observe a superposition of the individual loading scenarios investigated in the previous sections. Please note, that, similar to these previous section, the ranges of the axes are adjusted accordingly and therefore vary from plot to plot.

Cyclic tensile loading with increasing loading level. We conduct an analysis of the model response upon cyclic loading via uniaxial extension. We successively apply a normal strain ε_{11} to induce cyclic uniaxial loading in the $\boldsymbol{e}_1$-direction. We apply the strain ε_{11} in five cycles from 0 % to 5 % with an increasing magnitude of 1 % per cycle. For this analysis, we restrict to Puck case I. The resulting stress-strain curves and damage-strain curves are shown in Figure 14.

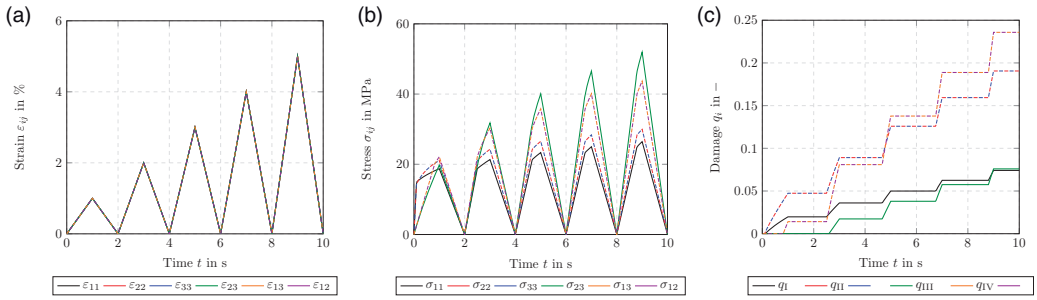

Figure 12. Step wise increase of multiaxial loading to evoke all stresses and damage functions simultaneously. (a) Strain vs. time. (b) Stress vs. time. (c) Damage evolution over time.

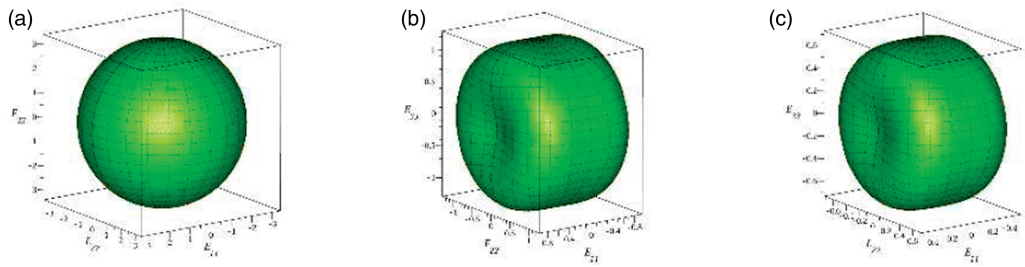

Figure 13. Evolution of an initially isotropic stiffness during multiaxial loading steps, visualized via YMS plots. (a) Strain 0%. (b) Strain 2%. (c) Strain 5%.

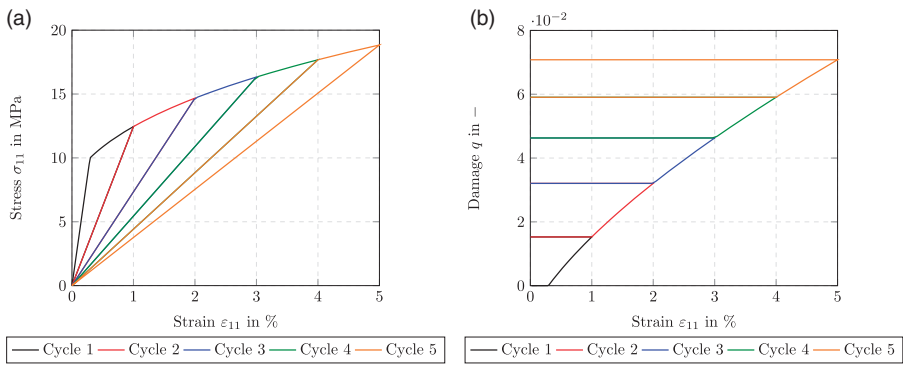

Figure 14. Cyclic tensile loading with increasing loading level for Puck case I. (a) Stress-strain curve. (b) Damage-strain curve.

Upon loading, the material behaves linear elastically until a specific critical stress threshold or the maximum stress of the previous cycle is reached, see Figure 14(a). During the in-between unloading to $\varepsilon_{11} = 0\,\%$ and reloading, the damage variables do not evolve further. Besides, the pure damaging character of the model is highlighted, as no remaining residual strains occur. The step wise evolution of the damage variable q is shown in Figure 14(b).

Note that the presented model is capable to predict damage onset upon both, tensile and compressive loading. Due to the definition of the damage functions the quadratic nature of the driving force $\mathbb{T}$ (2.18), the damage evolution is driven in similar fashions by both, tensile and compressive stresses. Considering a single damage variable q for, both, the tensile and the compressive regime, would lead to a combined damage evolution. Accounting for tension-compression asymmetry requires an extension of the model at hand, see the conclusion.

Model response for a continuous-fiber microstructure

Application of separate loading cases with Puck-type extraction tensors. After discussing the model response for homogeneous stress states, we account for heterogeneous stress states in two ways to show the basic feasibilities of our damage model. First, we shall investigate a microstructure with a continuous fiber reinforcement. In the next section, we will turn our attention to a mesoscale simulation.

To account for damage evolution in the matrix, we introduce two extraction tensor corresponding to the spherical and deviatoric projectors of fourth-order

$$\mathbb{B}_{\text{sph}} = \mathbb{P}_1 = \frac{1}{3}\boldsymbol{I} \otimes \boldsymbol{I}, \quad \mathbb{B}_{\text{dev}} = \mathbb{P}_2 = \mathbb{I}^{\text{S}} - \mathbb{P}_1, \tag{4.4}$$

that allow describing a damage evolution in response to dilatation and distortion. We use damage-activation functions based on these two extraction tensors (4.4) and corresponding damage parameters $\sigma_0 = 30$ MPa, $H = 130$ MPa and $m = 1$ for both cases. Furthermore, the matrix of the fiber-reinforced microstructure is endowed with the elastic properties of UPPH, as defined in Table 1. The fibers are modeled in a purely elastic fashion using the elastic moduli of E-glass, see Table 1. The continuous-fiber reinforced microstructure is geometrically modeled by 50 inclusions with a diameter of 13 μm and a total volume fraction of about 40 %. We generated the microstructure by the adaptive shrinking-cell algorithm of Torquato and Jiao (2010). The setup represents aligned fibers in a UPPH matrix as present in SMC composite bundles (Dumont et al., 2007; Kim et al., 2011; Meyer et al., 2020), where the fiber direction $\boldsymbol{e}_1$ coincides with the primary direction of the Puck cases.

In three different loading scenarios, we apply three different macroscopic strains via mixed boundary conditions, see Kabel et al. (2016) for details. For each scenario, we analyze the induced damage fields of the associated variables q_{sph} and q_{dev}. In scenario 1, we apply the macroscopic normal strain $\bar{\varepsilon}_{22}$ perpendicular to the fiber direction (in horizontal direction). In scenarios 2 and 3, we apply macroscopic shear strains $\bar{\varepsilon}_{12}$ and $\bar{\varepsilon}_{23}$, in fiber direction and transverse to the fiber direction, respectively.

The average runtime for a resolution of 256×256 pixels and 50 time steps was about 100 s on 12 threads. An accompanying resolution study is discussed in the following section. Figure 15 shows the damage fields for q_{sph} and q_{dev} for the introduced cases and corresponding to the different loading scenarios. Figure 15(a) shows that normal loading perpendicular to the fiber direction leads to a dilatation-triggered damage evolution in the respective direction, as a result of stress concentrations at the inclusion boundaries. As a consequence of the complexity of the induced stress state, damage due to distortion is initiated, as well, see Figure 15(a). In general, the stress level is higher for regions with more closely packed inclusions, inducing a significantly higher level of damage in those regions. Damage initiates at the inclusion boundaries and evolves in the loading direction, deflected by other inclusions. Shear loading in fiber direction leads to an associated damage evolution due to distortion, as shown in Figure 15(f). As the applied shear is oriented in fiber direction,

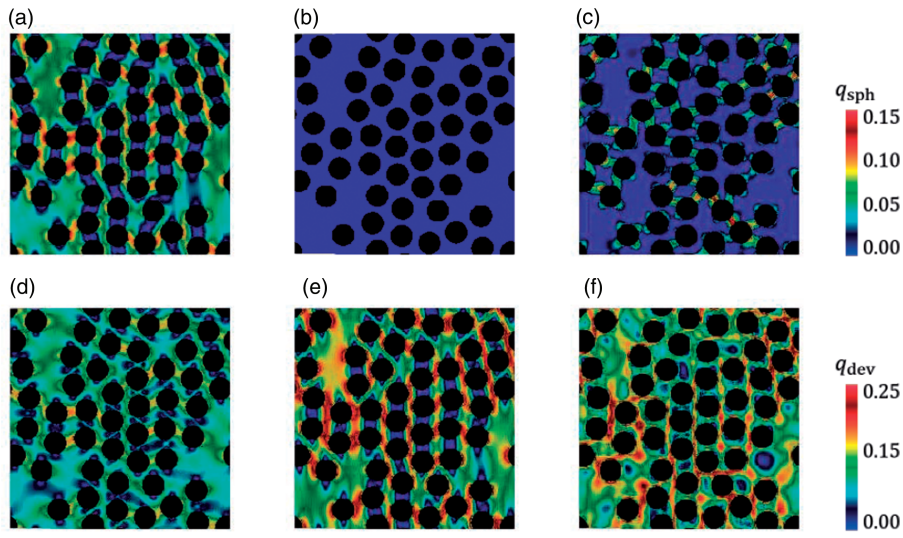

Figure 15. Model response for a continuous-fiber reinforced microstructure based on spherical and deviatoric damage and three different loading cases. (a) Loading $\bar{\varepsilon}_{22}$, q_{sph}. (b) Loading $\bar{\varepsilon}_{12}$, q_{sph}. (c) Loading $\bar{\varepsilon}_{23}$, q_{sph}. (d) Loading $\bar{\varepsilon}_{22}$, q_{dev}. (e) Loading $\bar{\varepsilon}_{12}$, q_{dev}. (f) Loading $\bar{\varepsilon}_{23}$, q_{dev}.

the deformation is not hindered by these fibers and spherical stresses do not occur. Hence, damage due to dilatation does not evolve, see Figure 15(b). Applying a macroscopic shear perpendicular to fiber direction evokes both, the evolution of damage due to spherical stresses, see Figure 15(c), as well as deviatoric stresses, see Figure 15(g).

Resolution study. The presented resolution study demonstrates that the proposed damage model leads to mesh-independent results even without gradient enhancement. This does not come by surprise, as we specifically designed such a hardening-type damage model. Still, even in the case of hardening, a resolution study is imperative to ensure mesh-independent results. In particular, we will justify the resolution employed in the previous section.

Figure 16 shows a continuous-fiber reinforced microstructure with the same properties as for Figure 15. We vary the resolution from 64×64 to 1024×1024 pixels. Similar to scenario 1, see Figure 15(a), we apply a macroscopic strain $\bar{\varepsilon}_{22}$ for all resolutions, so that both damage cases, i.e., dilatation and distortion, are being activated. The strain is successively increased from 0 % to 5 % within 50 equidistant loading steps.

The resulting distribution of the predominant damage variable q_{sph} for damage due to dilatation is shown in Figure 16. We observe that areas of low and high damage level are captured also for low resolution, but there are slight differences in the achieved damage level. Also, as expected, localization behavior is not evident. To get a more qualitative insight, the macroscopic stress-strain curves are shown in Figure 17(a). For a resolution of 64×64 pixels, the computed stresses are overestimated. For higher resolutions with 128×128 to 1024×1024 pixels, the differences are small. Investigating the relative deviations $\left(\bar{\sigma}_{22}^{\text{reso}} - \bar{\sigma}_{22}^{1024}\right)/\bar{\sigma}_{22}^{1024}$ of the computed effective stress $\bar{\sigma}_{22}$ relative to the stress at a resolution of 1024×1024, see Figure 17(b), we observe that, for resolutions with 256×256 pixels and higher, the deviations are below 1 %. The iteration counts and timings are collected in Table 2. The total outer iterations (including Newton and CG

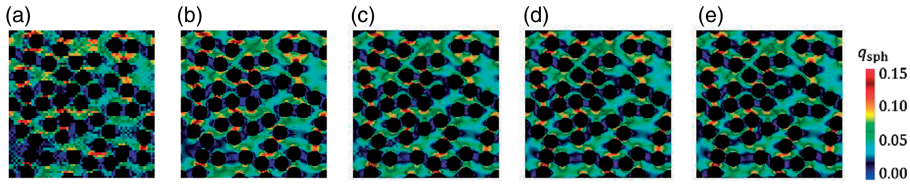

Figure 16. Model response for a continuous-fiber reinforced microstructure evaluated at five different resolutions. (a) 64^2. (b) 128^2. (c) 256^2. (d) 512^2. (e) 1024^2.

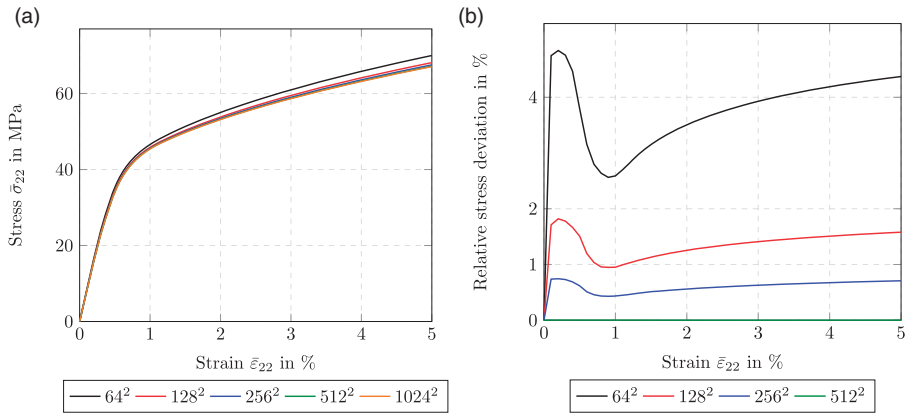

Figure 17. Resolution study for the continuous-fiber reinforced microstructure. (a) Stress-strain curve. (b) Relative stress deviation w. r. t. $\bar{\sigma}_{22}$ for 1024^2 pixels.

Table 2. Iterations and timings for the conducted resolution study.

	Iterations		Timings	
Resolution	Total outer	Max. average inner	t_{inner}	t_{total}
64^2	2 953	2.774	2 s	9 s
128^2	2 897	2.814	6 s	26 s
256^2	3 012	2.843	22 s	108 s
512^2	3 023	2.853	88 s	524 s
1024^2	2 987	2.858	352 s	1793 s

iterations) for all loading steps vary in a narrow window around approximately 2 950 for all resolutions considered. To give a comparable standard for the inner (material) iterations, we compute the average number of inner iterations over all voxels and subsequently take the maximum value over all loading steps. A value of about 2.8 inner iterations per voxel, irrespective of the resolution, indicates quadratic convergence of the Newton method. Both, the overall timing for computing all inner iterations, as well as the total timing, increase roughly with the degrees of freedom.

Based on this resolution study, a resolution of 256×256 pixels represents a compromise between an accurate prediction and a short runtime.

A Plain-weave composite under shear loading

Last but not least, we demonstrate the utility of our model framework for modeling anisotropic damage evolution in a woven fiber-reinforced composite. Simon et al. (2017) investigated the mechanical behavior of a plain-weave composite manufactured from continuous carbon fibers reinforcing an epoxy matrix resin, see Figure 18(a). The carbon fibers are aligned unidirectionally in fiber tows that are regularly interwoven. As each of these tows consists of thousands of carbon fibers, it is customary to work with a multiscale scheme that considers three different scales: the macroscopic scale is large compared to the woven unit cell, see Figure 18(a), which constitutes the mesoscale. Within the latter, the tows are considered homogeneous and anisotropic. On the microscale, the tows get resolved in terms of continuous carbon fibers in an epoxy resin.

The linear elastic moduli of the considered materials are listed in Table 3. These comprise the isotropic epoxy matrix and the transversely isotropic carbon fibers. The transversely isotropic engineering constants for the tows were obtained by linear elastic homogenization. Please note that the subscript "L" and "T" refer to longitudinal and transverse, respectively.

Based on earlier work (Bednarcyk et al., 2015, 2014; Stier et al., 2015), Simon et al. (2017) presented a regularized orthotropic continuum damage-model based on the framework developed by Barbero and co-workers (Barbero and Lonetti, 2002; Lonetti et al., 2003, 2004) and concisely summarized in his book (Barbero, 2013). More precisely, their strategy takes the orthotropic engineering constants as the point of departure, and models their degradation on an individual basis in terms of associated scalar damage variables. Based on the associated driving forces, damage surfaces are defined, together with appropriate kinetic laws.

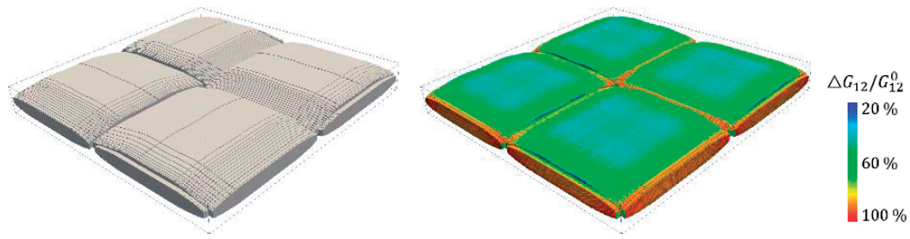

Figure 18. Microstructure and predicted relative reduction of the shear modulus G_{12} in a plain weave composite. (a) Voxelized weave microstructure with four tows. (b) Relative reduction (4.8) of shear modulus G_{12}.

Table 3. Elastic moduli of matrix, fibers and tows (Simon et al., 2017, Tables 1 and 2).

Constituent	Young's modulus in GPa	Shear modulus in GPa	Poisson's ratio
Epoxy	$E = 3$	$G = 1.09$	$\nu = 0.38$
Carbon fibers	$E_L = 290$	$G_{LT} = 20$	$\nu_{LT} = 0.2$
	$E_T = 20$	$G_{TT} = 9$	$\nu_{TT} = 0.11$
Tows	$E_L = 144$	$G_{LT} = 2.58$	$\nu_{LT} = 0.29$
	$E_T = 7.84$	$G_{TT} = 1.91$	$\nu_{TT} = 0.39$

Expressing the dependence of the stiffness tensor on the orthotropic engineering constants is most easily realized in terms of the compliance tensor, the approach of Simon et al. (2017) appears superficially similar to our approach. However, we do not fix the damage variables a priori. Rather, they emerge naturally in our framework based on the chosen extraction tensors and damage-activation functions.

In this paragraph, we demonstrate that our model is capable of reproducing the damage behavior upon quasi-static loading of the weave composite. The protocol we present is straightforward and proceeds step by step. As a first step, we introduce a number of extraction tensors which capture elementary damage cases evoked by pure normal- and shear-loading scenarios. The tensors extract the associated normal and shear stress components from the applied stress state $\boldsymbol{\sigma}$. These extraction tensors are uncoupled. Hence, damage in a certain direction is solely driven by the associated loading case, e. g., normal damage in $\boldsymbol{e}_1$-direction due to normal loading in $\boldsymbol{e}_1$-direction,

$$\mathbb{B}_{11} = \boldsymbol{e}_1^{\otimes 4}, \quad \mathbb{B}_{22} = \boldsymbol{e}_2^{\otimes 4}, \quad \mathbb{B}_{33} = \boldsymbol{e}_3^{\otimes 4}, \tag{4.5}$$

$$\mathbb{B}_{23} = (\boldsymbol{e}_2 \otimes_{\mathrm{S}} \boldsymbol{e}_3)^{\otimes 2}, \quad \mathbb{B}_{13} = (\boldsymbol{e}_1 \otimes_{\mathrm{S}} \boldsymbol{e}_3)^{\otimes 2}, \quad \mathbb{B}_{12} = (\boldsymbol{e}_1 \otimes_{\mathrm{S}} \boldsymbol{e}_2)^{\otimes 2}. \tag{4.6}$$

Combining suitable damage-activation functions based on these extraction tensors permit modeling a wide range of damage-evolution predictions. In particular, they enable us to describe the stiffness reduction for the scenario considered by Simon et al. (2017).

We first capture the damage evolution in a neat epoxy sample under non-monotonic uniaxial loading and choose an extraction tensor of type $(4.5)_1$. Subsequently, we account for the damage onset due to shear loading by using a second damage-activation function in combination with an extraction tensor of type $(4.6)_3$. The identified parameters for the epoxy damage-model are summarized in Table 4, which were chosen to reproduce the results of Simon et al. (2017) best.

Furthermore, we employ a number of damage-activation functions and suitable extraction tensors to capture the damage evolution in the fiber tows. We fix the longitudinal tow direction to correspond to the local $\boldsymbol{e}_1$-direction. The response to shear loading in longitudinal and transverse directions is best described with extraction tensors of the forms $(4.6)_1$ and $(4.6)_3$. As the reduction of the two orthotropic Young's moduli in the transverse plane (and hence the associated damage evolutions) is not identical, we introduce an additional extraction tensor

$$\mathbb{B} = 4\,\boldsymbol{e}_2^{\otimes 4} + \boldsymbol{e}_3^{\otimes 4}, \tag{4.7}$$

which is supplemented by a fourth damage-activation function with an extraction tensor that drives damage in $\boldsymbol{e}_2$-direction $(4.5)_2$ only. Table 4 comprises a complete list of the identified damage parameters. The listed extraction tensors and damage parameters at hand allow us to reproduce the structural behavior of, both, the neat epoxy and the tows, the latter in terms of stress-strain curves and the reduction of the orthotropic engineering constants. The corresponding results are shown in Figure 19.

With the introduced extraction tensors and damage parameters at hand, we are able to reproduce the experimental results obtained for the neat epoxy resin, as well es the predictions computed by Simon et al. (2017) quite accurately, see Figure 19(a). The decrease in the individual orthotropic engineering-constants are shown in Figure 19(b) to (d), where dashed lines correspond to our model and solid lines refer to the references Simon et al. (2017) and Bednarcyk et al. (2015). For all considered loading cases, our proposed modeling framework makes it simple to account for

Table 4. Extraction tensors and identified damage parameters to capture the mechanical behavior of epoxy and tow.

Constituent	Extraction tensor	σ_0 in MPa	H in MPa	m
Epoxy	$(4.5)_1$	0.5	180	0.47
	$(4.6)_3$	101	41	0.97
Tow	$(4.6)_1$	8	275	0.3
	$(4.6)_3$	10	245	0.3
	$(4.5)_2$	79	30	0.9
	(4.7)	200	630	0.4

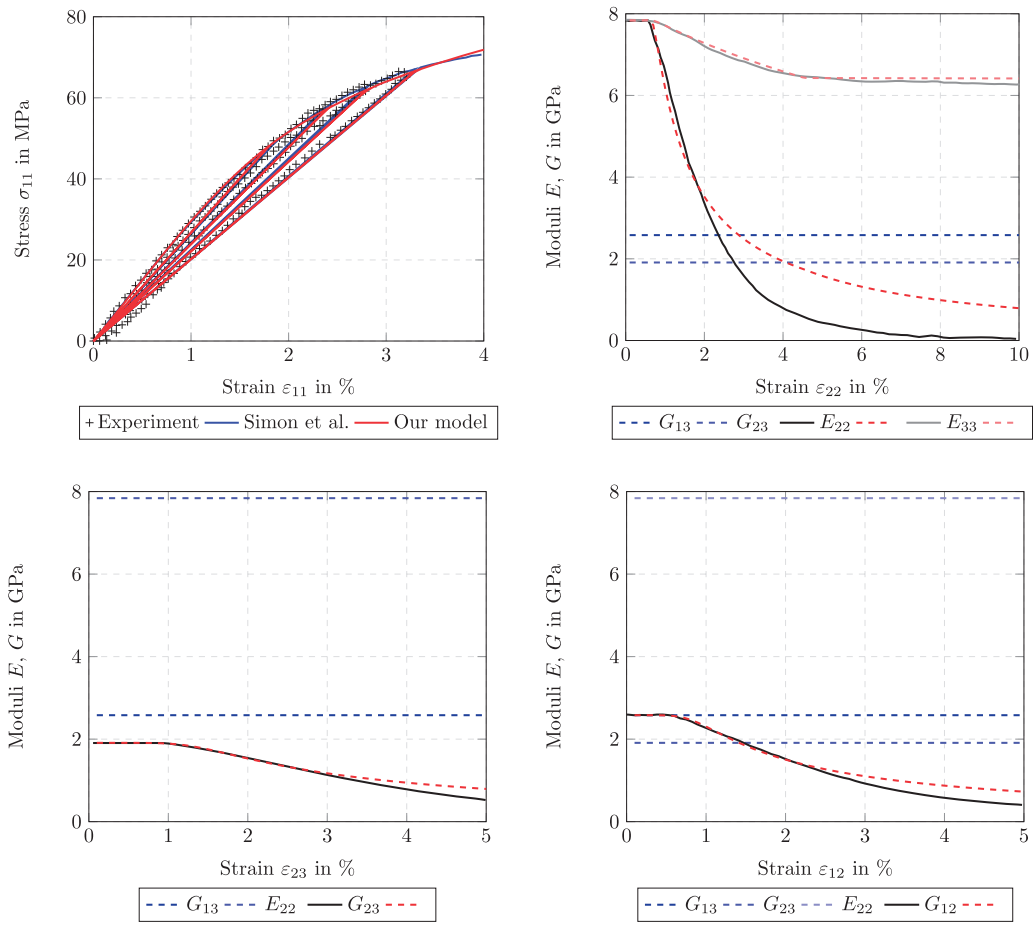

Figure 19. Comparison of predicted stress-strain curve and reductions of the orthotropic engineering constants based on introduced extraction tensors (see Table 4). Our model predictions are dashed in (b)–(d). (a) Neat epoxy behavior under normal loading. (b) Tow behavior under transverse normal loading. (c) Tow behavior under transverse shear loading. (d) Tow behavior under longitudinal shear loading.

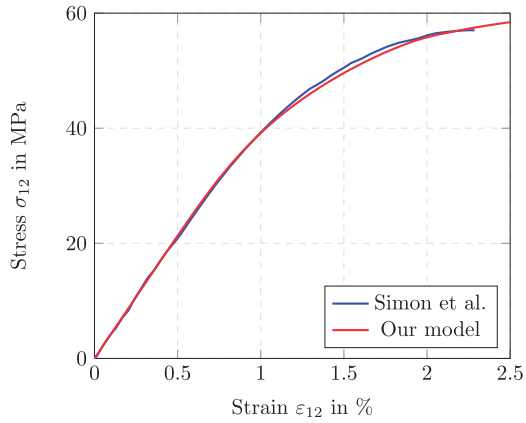

Figure 20. Comparison of effective stress-strain curves for plain weave under shear loading.

those engineering constants which remain unaffected during the loading. Figure 19(b) shows that the reduction of Young's modulus E_{33} is predicted correctly up to an applied strain of 10 %. The shear moduli are predicted quite well up to a strain level of 5 %, see Figure 19(c) and (d). Only the evolution of Young's modulus E_{22} shows some deviations beyond a strain level of 3 %, as our model is unable to capture the slope of reduction accurately enough for this case. To sum up, the proposed modeling framework permits reproducing the reduction of all affected engineering constants accurately for small deformations of up to 3 %. For the identified parameter set, we investigate the plain-weave composite that was also studied by Simon et al. (2017), see Figure 18(a). The meso-structure, with a required tow-volume fraction of approximately 75 %, was generated by a level-set approach developed by Sonon and co-workers (Sonon et al., 2012; Sonon and Massart, 2013; Wintiba et al., 2017) and discretized on a regular grid with $512 \times 512 \times 56$ voxels. Just as Simon et al. (2017), we investigate the longitudinal shear response of the plain-weave cell. For this purpose, we analyze the effective stress-strain curve, as well as the reduction of the shear modulus G_{12} measured in terms of the relative error

$$\triangle G_{12} = G_{12}^0 - G_{12} \tag{4.8}$$

w. r. t. the initial, undamaged shear modulus G_{12}^0. The predicted full-field distribution of this relative reduction is shown in Figure 18(b), and coincides well with the results presented by (Simon et al., 2017, Figure 9). Moreover, the effective stress-strain curves of the plain-weave composite subjected to longitudinal shear match well for the entire loading regime, see Figure 20.

Summary and conclusions

In this article, a generalized standard material (GSM) model for anisotropic damage evolution based on the compliance tensor as the primary damage variable was developed. Based on the insight that the Hookean elastic energy density, considered as a function of the elastic strain and the compliance tensor, is a convex function of both arguments, a convex framework for quasi-static damage evolution was established, preventing damage localization intrinsically. Indeed, by choosing the energy (density) related to the progressive degradation of the material appropriately, the condensed incremental

potential (Miehe, 2002) is strictly convex and of superlinear growth, which prevents localization for such a model. Of course, working with a softening-type energy for the damage-surface variables is also possible, and should be studied more closely in subsequent work.

The second section is organized to emphasize the modular fashion that the compliance-based damage model is built up. The model might be extended in subsequent work, for instance accounting for strain-rate sensitivity within the model. For an overview of the assumptions leading to specific specializations of the evolution of internal variables, we refer to the overview in Appendix A. The modeling framework is general enough to incorporate coupling to other inelastic models, such as plasticity or viscoplasticity (McDowell, 2008; Rousselier, 1979), entirely within the proposed framework. Also, due to its inherent stability, an extension to fatigue damage, as observed for certain fiber-reinforced polymers (Bartkowiak et al., 2019, 2020; Sauer and Richardson, 1980), appears promising (Magino et al., 2021).

The modular character of the model was exemplified by specific damage-extraction tensors motivated by Puck's anisotropic failure criteria (Knops, 2008; Puck and Schürmann, 2002). With these ingredients at hand, we demonstrated the model's capabilities of developing complex anisotropic stiffness states, not restricted a priori by a specific degree of (an)isotropy of the stiffness tensor, emphasizing that the model is capable of handling *any* initial stiffness. We also showed the model's capabilities on meso and volume-element scale, based upon a straightforward numerical treatment. With these achievements at hand, accounting for additional failure criteria (Bouhala et al., 2013; Fritzsche et al., 2008; Kaddour et al., 2004) or coupling the model to phase-field fracture models (Gerasimov and De Lorenzis, 2019; Miehe et al., 2010; Schneider et al., 2016a) appears possible.

Returning to our original motivation, i.e., modeling anisotropic damage of SMC composite materials, requires incorporating the presented modeling framework into a three-scale homogenization scheme (Anagnostou et al., 2018). The underlying fiber bundle mesostructure (Dumont et al., 2007; Meyer et al., 2020; Schöttl et al., 2019) has to be accounted for, and the model parameters have to be fitted to experimental data. For the latter purpose, a convenient experimental program is necessary (Schemmann et al., 2018c).

From a mathematical perspective, a thorough mathematical analysis of our model is desirable, whereas an extension to tension-compression asymmetry appears imperative in order to model load reversals.

Declaration of conflicting interests

The authors declared no potential conflicts of interest with respect to the research, authorship, and/or publication of this article.

Funding

The authors disclosed receipt of the following financial support for the research, authorship, and/or publication of this article: JG, MS and TB acknowledge financial support by the German Research Foundation (DFG) within the International Research Training Group "Integrated engineering of continuous-discontinuous long fiber reinforced polymer structures" (GRK 2078).

Acknowledgements

The support by the German Research Foundation (DFG) is gratefully acknowledged. We thank D. Wicht for preparing the plain-weave geometry and S. Gajek for fruitful discussions. We are grateful to the anonymous reviewers for their suggestions and their constructive feedback.

Authorship contribution statement

JG, MS and TB were responsible for the development of the model and methodology presented in this publication. Conceptualization was taken over by MS, AH and TB. The software implementation was done by JG and MS. Validation, investigation of the results, formal analysis and the subsequent visualization were performed by JG. Resources were provided by MS and TB. The original manuscript draft was written by JG and MS and extensively reviewed and edited by JG, MS, AH and TB. The research project was administrated by JG, MS and TB. Funding was acquired by MS and TB. The research was supervised by MS, AH and TB.

ORCID iD

Thomas Böhlke https://orcid.org/0000-0001-6884-0530

Note

1. Alternatively, representing $\mathbb{S}$ in matrix form, the inverse may also be represented as the adjugate matrix divided by the determinant, i.e., $\mathbb{S} \mapsto \mathbb{S}^{-1}$ is a rational function of the matrix entries.

References

Abu Al-Rub RK and Voyiadjis GZ (2009) Gradient-enhanced coupled plasticity-anisotropic damage model for concrete fracture: Computational aspects and applications. *International Journal of Damage Mechanics* 18(2): 115–154.

Abu-Farsakh GA and Asfa AM (2020) A unified damage model for fibrous composite laminae subject to in-plane stress-state and having multi material-nonlinearity. *International Journal of Damage Mechanics* 29(9): 1329–1344.

Advani SG and Tucker CL (1987) The use of tensors to describe and predict fiber orientation in short fiber composites. *Journal of Rheology* 31(8): 751–784.

Aifantis EC (1984) On the microstructural origin of certain inelastic models. *Journal of Engineering Materials and Technology* 106(4): 326–330.

Alabdullah M and Ghoniem NM (2020) A thermodynamics-based damage model for the non-linear mechanical behavior of SiC/SiC ceramic matrix composites in irradiation and thermal environments. *International Journal of Damage Mechanics* 29(10): 1569–1599.

Anagnostou D, Chatzigeorgiou G, Chemisky Y, et al. (2018) Hierarchical micromechanical modeling of the viscoelastic behavior coupled to damage in SMC and SMC-hybrid composites. *Composites Part B: Engineering* 151: 8–24.

Bakhshan H, Afrouzian A, Ahmadi H, et al. (2018) Progressive failure analysis of fiber-reinforced laminated composites containing a hole. *International Journal of Damage Mechanics* 27(7): 963–978.

Balzani D and Ortiz M (2012) Relaxed incremental variational formulation for damage at large strains with application to fiber-reinforced materials and materials with truss-like microstructures. *International Journal for Numerical Methods in Engineering* 92(6): 551–570.

Baranger E (2018) Extension of a fourth-order damage theory to anisotropic history: Application to ceramic matrix composites under a multi-axial non-proportional loading. *International Journal of Damage Mechanics* 27(2): 238–252.

Barbero EJ (2013) *Finite Element Analysis of Composite Materials Using Abaqus*. New York: CRC Press, Taylor and Francis Group, LLC.

Barbero EJ and Lonetti P (2002) An inelastic damage model for fiber reinforced laminates. *Journal of Composite Materials* 36(8): 941–962.

Bartkowiak M, Liebig W and Weidenmann KA (2020) Fatigue damage behavior of continuous-discontinuous fiber reinforced sheet molding compounds. In: Hausmann JM, Siebert M, von Hehl A et al. (eds.) *Proceedings of the 4th International Conference Hybrid 2020 Materials and Structures, Web-Conference, Germany*. DGM - Deutsche Gesellschaft für Materialkunde e.V., pp. 1–7.

Bartkowiak M, Weit H, Montesano J, et al. (2019), Characterization of discontinuous fiber reinforced sheet molding compounds under tension-tension fatigue load. In: Kalaitzidou K (ed) *American Society for Composite - 34th Technical Conference on Composite Materials*, Atlanta, USA. Vol. 28428. DEStech Publications, pp. 3–10.

Bažant ZP (1991) Why continuum damage is nonlocal: Micromechanics arguments. *Journal of Engineering Mechanics* 117(5): 1070–1087.

Becker R, Needleman A, Richmond O, et al. (1988) Void growth and failure in notched bars. *Journal of the Mechanics and Physics of Solids* 36(3): 317–351.

Bednarcyk BA, Stier B, Simon JW, et al. (2014) Damage analysis of composites using a three-dimensional damage model: Micro-scale architectural effects. In: *American Society for Composites 29th Technical Conference*. La Jolla, USA: Curran, Vol. 513. pp. 1–19.

Bednarcyk BA, Stier B, Simon JW, et al. (2015) Meso- and micro-scale modeling of damage in plain weave composites. *Composite Structures* 121: 258–270.

Behnel S, Bradshaw R, Citro C, et al. (2011) Cython: The best of both worlds. *Computing in Science & Engineering* 13(2): 31–39.

Belytschko T, Bažant Z P, Yul-Woong H, et al. (1986) Strain-softening materials and finite-element solutions. *Computers & Structures* 23(2): 163–180.

Beremin FM, Pineau A, Mudry F, et al. (1983) A local criterion for cleavage fracture of a nuclear pressure vessel steel. *Metallurgical Transactions A* 14(11): 2277–2287.

Bergounioux M, Haddou M, Hintermüller M, et al. (2000) A comparison of a Moreau–Yosida-based active set strategy and interior point methods for constrained optimal control problems. *SIAM Journal on Optimization* 11(2): 495–521.

Bergounioux M, Ito K and Kunisch K (1999) Primal-dual strategy for constrained optimal control problems. *SIAM Journal on Control and Optimization* 37(4): 1176–1194.

Bertram A (2011) *Elasticity and Plasticity of Large Deformations*. Berlin/Heidelberg: Springer-Verlag.

Bhattacharyya M, Dureisseix D and Faverjon B (2020) Numerical homogenisation based on asymptotic theory and model reduction for coupled elastic-viscoplastic damage. *International Journal of Damage Mechanics* 29(9): 1416–1444.

Böhlke T and Brüggemann C (2001) Graphical representation of the generalized Hooke's law. *Technische Mechanik* 21(2): 145–158.

Borwein J and Lewis A (2006) *Convex Analysis and Nonlinear Optimization: Theory and Examples*. New York: Springer.

Bouhala L, Makradi A, Belouettar S, et al. (2013) Modelling of failure in long fibres reinforced composites by X-FEM and cohesive zone model. *Composites Part B: Engineering* 55: 352–361.

Brünig M and Ricci S (2005) Nonlocal continuum theory of anisotropically damaged metals. *International Journal of Plasticity* 21(7): 1346–1382.

Chaboche JL (1981) Continuous damage mechanics – A tool to describe phenomena before crack initiation. *Nuclear Engineering and Design* 64(2): 233–247.

Chaboche JL (1993) Development of continuum damage mechanics for elastic solids sustaining anisotropic and unilateral damage. *International Journal of Damage Mechanics* 2(4): 311–329.

Chaboche JL (2008) A review of some plasticity and viscoplasticity constitutive theories. *International Journal of Plasticity* 24(10): 1642–1693.

Chen Q, Zhu H, Ju JW, et al. (2018) Stochastic micromechanical predictions for the effective properties of concrete considering the interfacial transition zone effects. *International Journal of Damage Mechanics* 27(8): 1252–1271.

Cicekli U, Voyiadjis GZ and Abu Al-Rub RK (2007) A plasticity and anisotropic damage model for plain concrete. *International Journal of Plasticity* 23(10-11): 1874–1900.

De Borst R (1996) Softening, damage and higher-order continua. *Proceedings of the 2nd Conference on Fracture Mechanics of Concrete Structures* 1: 1631 –1640.

Desmorat R (2016) Anisotropic damage modeling of concrete materials. *International Journal of Damage Mechanics* 25(6): 818–852.

Dougill JW (1976) On stable progressively fracturing solids. *Zeitschrift Für Angewandte Mathematik Und Physik Zamp* 27(4): 423–437.

Drugan WJ and Willis JR (1996) A micromechanics-based nonlocal constitutive equations and estimates of representative volume element size for elastic composites. *Journal of the Mechanics and Physics of Solids* 44(4): 497–524.

Dumont P, Orgéas L, Favier D, et al. (2007) Compression moulding of SMC: In situ experiments, modelling and simulation. *Composites Part A: Applied Science and Manufacturing* 38(2): 353–368.

Fassin M, Eggersmann R, Wulfinghoff S, et al. (2019) Gradient-extended anisotropic brittle damage modeling using a second order damage tensor – Theory, implementation and numerical examples. *International Journal of Solids and Structures* 167: 93–126.

Fitoussi J, Bourgeois N, Guo G, et al. (1996) Prediction of the anisotropic damaged behavior of composite materials: Introduction of multilocal failure criteria in a micro-macro relationship. *Computational Materials Science* 5(1-3): 87–100.

Fitoussi J, Guo G and Baptiste D (1998) A statistical micromechanical model of anisotropic damage for S.M. C. composites. *Composites Science and Technology* 58(5): 759–763.

Forest S, Berdin C, Besson J, et al. (2004) *Local Approach to Fracture*. Paris: Les Presses de l'Ecole des Mines.

Franko M, Sedlaček M, Podgornik B, et al. (2017) Validation of linear damage rules using random loading. *International Journal of Damage Mechanics* 26(3): 463–469.

Frigo M and Johnson SG (2005) The design and implementation of FFTW3. *Proceedings of the IEEE* 93: 216–231.

Fritzsche P, Weder M, Wyss I, et al. (2008) A procedure for the simulation of failure in thermoplastic composites. *Composite Structures* 85(4): 337–349.

Ganjiani M (2018) A thermodynamic consistent rate-dependent elastoplastic-damage model. *International Journal of Damage Mechanics* 27(3): 333–356.

Gélébart L and Mondon-Cancel R (2013) Non-linear extension of FFT-based methods accelerated by conjugate gradients to evaluate the mechanical behavior of composite materials. *Computational Materials Science* 77: 430–439.

Gerasimov T and De Lorenzis L (2019) On penalization in variational phase-field models of brittle fracture. *Computer Methods in Applied Mechanics and Engineering* 354: 990–1026.

Germain N, Besson J and Feyel F (2007) Composite layered materials: Anisotropic nonlocal damage models. *Computer Methods in Applied Mechanics and Engineering* 196(41-44): 4272–4282.

Gitman IM, Askes H and Sluys L (2007) Representative volume: Existence and size determination. *Engineering Fracture Mechanics* 74(16): 2518–2534.

Goidescu C, Welemane H, Pantale O, et al. (2015) Anisotropic unilateral damage with initial orthotropy: A micromechanics-based approach. *International Journal of Damage Mechanics* 24(3): 313–337.

Görthofer J, Meyer N, Pallicity TD, et al. (2019) Virtual process chain of sheet molding compound: Development, validation and perspectives. *Composites Part B: Engineering* 169: 133–147.

Govindjee S, Kay GJ and Simo JC (1995) Anisotropic modelling and numerical simulation of brittle damage in concrete. *International Journal for Numerical Methods in Engineering* 38(21): 3611–3633.

Guo G, Fitoussi J, Baptiste D, et al. (1997) Modelling of damage behavior of a short-fiber reinforced composite structure by the finite element analysis using a micro-macro law. *International Journal of Damage Mechanics* 6(3): 278–299.

Gurson AL (1977) Continuum theory of ductile rupture by void nucleation and growth: Part I—Yield criteria and flow rules for porous ductile media. *Journal of Engineering Materials and Technology* 99(1): 2–15.

Halphen N and Nguyen Q (1975) Sur les matériaux standards generalisés. *Journal de Mécanique* 14: 508–520.

Hansen NR and Schreyer HL (1994) A thermodynamically consistent framework for theories of elastoplasticity coupled with damage. *International Journal of Solids and Structures* 31(3): 359–389.

Haupt P (2000) *Continuum Mechanics and Theory of Materials*. Berlin: Springer.

Hibbeler RC (2001) *Engineering Mechanics*. Pearson Education.

Hill R (1963) Elastic properties of reinforced solids: Some theoretical principles. *Journal of the Mechanics and Physics of Solids* 11(5): 357–372.

Hintermüller M, Ito K and Kunisch K (2002) The primal-dual active set strategy as a semismooth newton method. *SIAM Journal on Optimization* 13(3): 865–888.

Jin W and Arson C (2018) Micromechanics based discrete damage model with multiple non-smooth yield surfaces: Theoretical formulation, numerical implementation and engineering applications. *International Journal of Damage Mechanics* 27(5): 611–639.

Ju JW (1989) On energy-based coupled elastoplastic damage theories: Constitutive modeling and computational aspects. *International Journal of Solids and Structures* 25(7): 803–833.

Ju JW and Wu Y (2016) Stochastic micromechanical damage modeling of progressive fiber breakage for longitudinal fiber-reinforced composites. *International Journal of Damage Mechanics* 25(2): 203–227.

Junker P, Riesselmann J and Balzani D (2021) Efficient and robust numerical treatment of a gradient-enhanced damage model at large deformations. Available at: http://arxiv.org/abs/2102.08819 (accessed 17 May 2021).

Junker P, Schwarz S, Jantos DR, et al. (2019) A fast and robust numerical treatment of a gradient-enhanced model for brittle damage. *International Journal for Multiscale Computational Engineering* 17(2): 151–180.

Kabel M, Böhlke T and Schneider M (2014) Efficient fixed point and Newton–Krylov solvers for FFT-based homogenization of elasticity at large deformations. *Computational Mechanics* 54(6): 1497–1514.

Kabel M, Fliegener S and Schneider M (2016) Mixed boundary conditions for FFT-based homogenization at finite strains. *Computational Mechanics* 57(2): 193–210.

Kaddour AS, Hinton MJ and Soden PD (2004) A comparison of the predictive capabilities of current failure theories for composite laminates: Additional contributions. *Composites Science and Technology* 64(3-4): 449–476.

Kanit T, Forest S, Galliet I, et al. (2003) Determination of the size of the representative volume element for random composites: Statistical and numerical approach. *International Journal of Solids and Structures* 40(13-14): 3647–3679.

Kehrer L, Wicht D, Wood JT, et al. (2018) Dynamic mechanical analysis of pure and fiber-reinforced thermoset- and thermoplastic-based polymers and free volume-based viscoelastic modeling. *GAMM-Mitteilungen* 41(1): e201800007.

Khayyam Rayeni H, Mazaheri AH and Taheri-Behrooz F (2020) Strength prediction of woven composite rings using progressive damage modeling. *International Journal of Damage Mechanics* 29(6): 851–873.

Kim MS, Lee WI, Han WS, et al. (2011) Optimization of location and dimension of SMC pre-charge in compression molding process. *Computers and Structures* 89(15–16): 353–368.

Kim IB, Ri CS and So YI (2016) A damage mechanics model of materials with voids and cracks. *International Journal of Damage Mechanics* 25(6): 773–796.

Knops M (2008) *Analysis of Failure in Fiber Polymer Laminates: The Theory of Alfred Puck*. Berlin, Heidelberg and New York: Springer Science & Business Media.

Krajcinovic D (1984) Continuum damage mechanics. *Applied Mathematics Reviews* 37: 1–6.

Krajcinovic D (1989) Damage mechanics. *Mechanics of Materials* 8(2-3): 117–3679.

Ladevèze P (1983) On an anisotropic damage theory. *Proceedings of the CNRS* 351: 355–363.

Ladevèze P (2002) An anisotropic damage theory with unilateral effects: Applications to laminates and to three-and four-dimensional composites. In: Allix O and Hild F (eds) *Continuum Damage Mechanics of Materials and Structures*. Oxford: Elsevier, pp. 205–234.

Ladevèze P, Baranger E, Genet M, et al. (2014), Damage and lifetime modeling for structure computations. In: Bansal NP and Lamon J (eds) *Ceramic Matrix Composites: Materials, Modeling and Technology*. New Jersey: Wiley, pp. 465–519.

Ladeveze P and Lemaitre J (1984) Damage effective stress in quasi unilateral conditions. In: *Proceedings of the 16th International congress of theoretical and applied mechanics*, Lyngby, Denmark.

Lemaitre J (1986) Local approach of fracture. *Engineering Fracture Mechanics* 25(5-6): 523–537.

Lemaitre J (1996) *A Course on Damage Mechanics*. 2nd ed. Berlin: Springer.

Lemaitre J and Chaboche JL (1990) *Mechanics of Solid Materials*. Cambridge: Cambridge University Press.

Li X, Qu X, Qi C, et al. (2020) An analytical model of multi-stress drops triggered by localized microcrack damage in brittle rocks during progressive failure. *International Journal of Damage Mechanics* 29(9): 1345–1360.

Li WS and Wu JY (2018) A consistent and efficient localized damage model for concrete. *International Journal of Damage Mechanics* 27(4): 541–567.

Liang S, Ren X and Li J (2018) A mesh-size-objective modeling of quasi-brittle material using micro-cell informed damage law. *International Journal of Damage Mechanics* 27(6): 913–936.

Liu D, He M and Cai M (2018) A damage model for modeling the complete stress–strain relations of brittle rocks under uniaxial compression. *International Journal of Damage Mechanics* 27(7): 1000–1019.

Liu XZ, Zhu HH, Ju JW, et al. (2020) Investigation of the unbiased probabilistic behavior of the fiber-reinforced concrete's elastic moduli using stochastic micromechanical approach. *International Journal of Damage Mechanics* 29(7): 1059–1075.

Lonetti P, Barbero EJ, Zinno R, et al. (2004) Erratum: Interlaminar damage model for polymer matrix composites. *Journal of Composite Materials* 38(9): 799–800.

Lonetti P, Zinno R, Greco F, et al. (2003) Interlaminar damage model for polymer matrix composites. *Journal of Composite Materials* 37(16): 1485–1504.

Luo Q, Liu D, Qiao P, et al. (2020) Micro-CT-based micromechanics and numerical homogenization for effective elastic property of ultra-high performance concrete. *International Journal of Damage Mechanics* 29(1): 45–66.

Magino N, Andrä H, Welschinger F, et al. (2021) A multiscale high-cycle fatigue-damage model for the stiffness degradation of fiber-reinforced materials based on a mixed variational framework. *Computer Methods in Applied Mechanics and Engineering*, submitted, 1-29.

McDowell D (2008) Viscoplasticity of heterogeneous metallic materials. *Materials Science and Engineering: R: Reports* 62(3): 67–123.

Meraghni F and Benzeggagh ML (1995) Micromechanical modelling of matrix degradation in randomly oriented discontinuous-fibre composites. *Composites Science and Technology* 55(2): 171–186.

Meyer N, Schöttl L, Bretz L, et al. (2020) Direct bundle simulation approach for the compression molding process of sheet molding compound. *Composites Part A: Applied Science and Manufacturing* 132: 105809.

Miehe C (2002) Strain-driven homogenization of inelastic microstructures and composites based on an incremental variational formulation. *International Journal for Numerical Methods in Engineering* 55(11): 1285–1322.

Miehe C, Welschinger F and Hofacker M (2010) Thermodynamically consistent phase-field models of fracture: Variational principles and multi-field FE implementations. *International Journal for Numerical Methods in Engineering* 83(10): 1273–1311.

Mohr O (1900) Welche umstände bedingen die elastizitätsgrenze und den bruch eines materials. *Zeitschrift Des Vereins Deutscher Ingenieure* 46(1524-1530): 1572–1577.

Moradi M, Bagherieh AR and Esfahani MR (2020) Constitutive modeling of steel fiber-reinforced concrete. *International Journal of Damage Mechanics* 29(3): 388–412.

Murakami S (2012) *Continuum Damage Mechanics: A Continuum Mechanics Approach to the Analysis of Damage and Fracture, Solid Mechanics and Its Applications*. Vol.185. Dordrecht: Springer.

Murakami S and Ohno N (1981) A continuum theory of creep and creep damage. In: Ponter ARS and Hayhurst DR (eds.) *Creep in Structures*. Berlin, Heidelberg: Springer Berlin Heidelberg, pp. 422–444.

Nasab AS and Mashayekhi M (2019) Application of an efficient anisotropic damage model to the prediction of the failure of metal forming processes. *International Journal of Damage Mechanics* 28(10): 1556–1579.

Okabe T, Onodera S, Kumagai Y, et al. (2018) Continuum damage mechanics modeling of composite laminates including transverse cracks. *International Journal of Damage Mechanics* 27(6): 877–895.

Onodera S and Okabe T (2020) Analytical model for determining effective stiffness and mechanical behavior of polymer matrix composite laminates using continuum damage mechanics. *International Journal of Damage Mechanics* 29(10): 1512–1542.

Ortiz M (1985) A constitutive theory for the inelastic behavior of concrete. *Mechanics of Materials* 4(1): 67–93.

Ortiz M and Popov EP (1982) A physical model for inelasticity of concrete. *Proceedings of the Royal Society A* 383: 101–125.

Pijaudier-Cabot G and Bažant ZP (1987) Nonlocal damage theory. *Journal of Engineering Mechanics* 113(10): 1512–1533.

Puck A and Schürmann H (2002) Failure analysis of FRP laminates by means of physically based phenomenological models. *Composites Science and Technology* 62(12-13): 1633–1662.

Pupurs A and Varna J (2017) Steady-state energy release rate for fiber/matrix interface debond growth in unidirectional composites. *International Journal of Damage Mechanics* 26(4): 560–587.

Rahimi AS, Ayatollahi MR and Torabi AR (2020) Elastic–plastic damage prediction in notched epoxy resin specimens under mixed mode I/II loading using two virtual linear elastic failure criteria. *International Journal of Damage Mechanics* 29(7): 1100–1116.

Ramtani S, Berthaud Y and Mazars J (1992) Orthotropic behavior of concrete with directional aspects: Modelling and experiments. *Nuclear Engineering and Design* 133(1): 97–111.

Reese S, Brepols T, Fassin M, et al. (2021) Using structural tensors for inelastic material modeling in the finite strain regime – A novel approach to anisotropic damage. *Journal of the Mechanics and Physics of Solids* 146: 104174.

Roubíček T (2009) Rate-independent processes in viscous solids at small strains. *Mathematical Methods in the Applied Sciences* 32(7): 825–862.

Rousselier G (1979) Contribution to the research on fracture properties of metals in the elasto-plastic field. *Bulletin de la Direction Des Etudes et Recherches. Serie A, Nucleaire, Hydraulique, Thermique* : 1–191.

Sauer JA and Richardson GC (1980) Fatigue of polymers. *International Journal of Fracture* 16(6): 499–532.

Schemmann M, Gajek S and Böhlke T (2018a) Biaxial tensile tests and microstructure-based inverse parameter identification of inhomogeneous SMC composites. In: Altenbach H, Jablonski F, Müller WH, et al. (eds) *Advances in Mechanics of Materials and Structural Analysis: In Honor of Reinhold Kienzler*. Vol. 80. Cham: Springer International Publishing, pp. 329–342.

Schemmann M, Görthofer J, Seelig T, et al. (2018b) Anisotropic meanfield modeling of debonding and matrix damage in SMC composites. *Composites Science and Technology* 161: 143–158.

Schemmann M, Lang J, Helfrich A, et al. (2018c) Cruciform specimen design for biaxial tensile testing of SMC. *Journal of Composites Science* 2(1): 12.

Schmidt T and Balzani D (2016) Relaxed incremental variational approach for the modeling of damage-induced stress hysteresis in arterial walls. *Journal of the Mechanical Behavior of Biomedical Materials* 58: 149–162.

Schneider M (2019) On the Barzilai-Borwein basic scheme in FFT-based computational homogenization. *International Journal for Numerical Methods in Engineering* 118(8): 482–494.

Schneider M, Ospald F and Kabel M (2016b) Computational homogenization of elasticity on a staggered grid. *International Journal for Numerical Methods in Engineering* 105(9): 693–720.

Schneider D, Schoof E, Huang Y, et al. (2016a) Phase-field modeling of crack propagation in multiphase systems. *Computer Methods in Applied Mechanics and Engineering* 312: 186–195.

Schöttl L, Weidenmann KA, Sabiston T, et al. (2019) Fiber bundle tracking method to analyze sheet molding compound microstructure based on computed tomography images. *Independent Nondestructive Testing and Evaluation International, Submitted Manuscript* : 1–12.

Schwarz S, Junker P and Hackl K (2021) Variational regularization of damage models based on the emulated RVE. *Continuum Mechanics and Thermodynamics* 33(1): 69–95.

Sharma A and Daggumati S (2020) Computational micromechanical modeling of transverse tensile damage behavior in unidirectional glass fiber-reinforced plastic composite plies: Ductile versus brittle fracture mechanics approach. *International Journal of Damage Mechanics* 29(6): 943–964.

Simo JC and Hughes TJR (1998) *Computational Inelasticity*. New York: Springer.

Simo J and Ju J (1987) Strain- and stress-based continuum damage models – I. Formulation. *International Journal of Solids and Structures* 23(7): 821–840.

Simon JW, Höwer D, Stier B, et al. (2017) A regularized orthotropic continuum damage model for layered composites: Intralaminar damage progression and delamination. *Computational Mechanics* 60(3): 445–463.

Sonon B, François B and Massart TJ (2012) A unified level set based methodology for fast generation of complex microstructural multi-phase RVEs. *Computer Methods in Applied Mechanics and Engineering* 223-224: 103–122.
Sonon B and Massart TJ (2013) A level-set based representative volume element generator and XFEM simulations for textile and 3D-reinforced composites. *Materials (Basel, Switzerland)* 6(12): 5568–5592.
Stier B, Bednarcyk BA, Simon JW, et al. (2015) Investigation of micro-scale architectural effects on damage of composites. National Aeronautics and Space Administration: NASA/TM-2015-218740, NASA Scientific and Technical Information Program. NASA Langley Research Center, Hampton, USA.
Susu LM (2017) *Analysis and optimal control of a damage model with penalty*. Doctoral thesis, Technische Unversität Dortmund, Fakultät für Mathematik.
Thomas M and Mielke A (2010) Damage of nonlinearly elastic materials at small strain – Existence and regularity results. *ZAMM* 90(2): 88–112.
Torquato S and Jiao Y (2010) Robust algorithm to generate a diverse class of dense disordered and ordered sphere packings via linear programming. *Physical Review E: Statistical, Nonlinear, and Soft Matter Physics* 82(6 Pt 1): 061302.
Trauth A, Pinter P and Weidenmann K (2017) Investigation of quasi-static and dynamic material properties of a structural sheet molding compound combined with acoustic emission damage analysis. *Journal of Composites Science* 1(2): 18.
Tvergaard V (1982) Material failure by void coalescence in localized shear bands. *International Journal of Solids and Structures* 18(8): 659–672.
Voyiadjis GZ (ed.) (2015) *Handbook of Damage Mechanics*. New York, NY: Springer New York.
Wang S and Xu W (2020) A coupled elastoplastic anisotropic damage model for rock materials. *International Journal of Damage Mechanics* 29(8): 1222–1245.
Wardeh MA and Toutanji HA (2017) Parameter estimation of an anisotropic damage model for concrete using genetic algorithms. *International Journal of Damage Mechanics* 26(6): 801–825.
Wei Q, Gu B and Sun B (2020) Ballistic penetration damages and energy absorptions of stacked cross-plied composite fabrics and laminated panels. *International Journal of Damage Mechanics* 29(9): 1465–1484.
Wicht D, Schneider M and Böhlke T (2020) On Quasi-Newton methods in fast Fourier transform-based micromechanics. *International Journal for Numerical Methods in Engineering* 121(8): 1665–1694.
Wintiba B, Sonon B, Ehab Moustafa Kamel K, et al. (2017) An automated procedure for the generation and conformal discretization of 3D woven composites RVEs. *Composite Structures* 180: 955–971.
Wu Y and Ju JW (2017) Elastoplastic damage micromechanics for continuous fiber-reinforced ductile matrix composites with progressive fiber breakage. *International Journal of Damage Mechanics* 26(1): 4–27.
Wulfinghoff S, Fassin M and Reese S (2017) A damage growth criterion for anisotropic damage models motivated from micromechanics. *International Journal of Solids and Structures* 121: 21–32.
Xu X, Gao F and Zhang Z (2018) Thermo-mechanical coupling damage constitutive model of rock based on the Hoek–Brown strength criterion. *International Journal of Damage Mechanics* 27(8): 1213–1230.
Yan H, Jin H and Yao R (2020) Prediction of the damage and fracture of cast steel containing pores. *International Journal of Damage Mechanics* 29(1): 166–183.
Yang Y, Chen J and Huang Z (2020) Damage evolution in fibrous composites caused by interfacial debonding. *International Journal of Damage Mechanics* 29(1): 67–85.
Yang L, Liu J, Yu B, et al. (2017) Failure path-independent methodology for structural damage evolution and failure mode analysis of framed structures. *International Journal of Damage Mechanics* 26(2): 274–292.
Yazdani S and Schreyer HL (1990) Combined plasticity and damage mechanics model for plain concrete. *Journal of Engineering Mechanics* 116(7): 1435–1450.
Zhang W and Cai Y (2010) *Continuum Damage Mechanics and* Numerical Applications. Berlin: Springer.
Zhang Y, Ju JW, Zhu H, et al. (2019) A novel damage model based on micromechanics for hybrid fiber reinforced cementitious composites under uniaxial compression. *International Journal of Damage Mechanics* 28(7): 1095–1132.

Appendix A: Summary of formulations for evolution equations

In this appendix, we give a short overview on the formulations regarding the evolution of the internal variables. The specification of the introduced model and the level of detail are increased from the general formulation (2.4) up to the evolution equations (2.30). For the sake of completeness, the corresponding KKT-conditions (2.23) are added.

<table>
<tr><th colspan="2">Summary of formulations for evolution equations for internal variables</th></tr>
<tr><td>General formulation

(2.4) : $\dot{z} \in \partial\Phi^* \left(-\dfrac{\partial w}{\partial z}(\boldsymbol{\varepsilon}, z) \right)$</td><td>$z = (\mathbb{S}, q)$ (2.9)

(2.19) : $(\dot{\mathbb{S}}, \dot{q}) \in \partial\Phi^* (\mathbb{T}, \beta)$</td></tr>
<tr><td>$\Phi^* \longleftrightarrow \phi_i$ (2.20)

$(2.21)_1$: $\dot{\mathbb{S}} = \sum_{i=1}^{M} \dot{\mu}_i \dfrac{\partial \phi_i(\mathbb{T}, \beta)}{\partial \mathbb{T}}$

$(2.21)_2$: $\dot{q} = \sum_{i=1}^{M} \dot{\mu}_i \dfrac{\partial \phi_i(\mathbb{T}, \beta)}{\partial \beta}$</td><td>$\phi_i(\mathbb{T}, \beta)$ (2.25)

$(2.30)_1$: $\dot{\mathbb{S}} = 2 \sum_{i=1}^{M} \dot{\mu}_i \, \mathbb{B}_i^2$

$(2.30)_2$: $\dot{q}_i = \dot{\mu}_i H_i, \quad i = 1, \ldots, M$</td></tr>
<tr><td colspan="2">Karush-Kuhn-Tucker (KKT) conditions

(2.23) : $\dot{\mu}_i \geq 0, \quad \phi_i(\mathbb{T}, \beta) \leq 0, \quad \dot{\mu}_i \, \phi_i(\mathbb{T}, \beta) = 0, \quad i = 1, \ldots, M$</td></tr>
<tr><td colspan="2">Express KKT conditions in terms of $\boldsymbol{\sigma}$ and q_i (2.28), (2.32)

(2.33) : $\dot{q}_i \geq 0, \quad f_i(\boldsymbol{\sigma}, q_i) \leq 0, \quad \dot{q}_i \, f_i(\boldsymbol{\sigma}, q_i) = 0, \quad i = 1, \ldots, M$</td></tr>
</table>

Appendix B: Convexity of the Hookean elastic energy density

In this appendix, we compute the Hessian of the Hookean elastic energy (density) w_e, see formula (2.11). For a twice (Frèchet) differentiable function $f : U \subseteq X \to \mathbb{R}$ on an open subset of a (Banach) vector space, the Hessian at some point $x \in U$ may be represented as a quadratic form

$$D^2 f(x) : X \to \mathbb{R}, \tag{B.1}$$

which may be computed by the directional second derivative

$$D^2 f(x)[y] = \frac{1}{2}\frac{\mathrm{d}^2}{\mathrm{d}\lambda^2} f(x+\lambda y)|_{\lambda=0}. \tag{B.2}$$

For our problem at hand, we have $U = \mathrm{Sym}(d) \times \mathcal{S}_d$ and $X = \mathrm{Sym}(d) \times \mathrm{Sym}(\mathrm{Sym}(d))$. Then, the Hessian of the elastic energy (2.11)

$$\begin{aligned} w_e &: \mathrm{Sym}(d) \times \mathcal{S}_d \to \mathbb{R} \\ w_e(\boldsymbol{\varepsilon}, \mathbb{S}) &= \frac{1}{2}\,\boldsymbol{\varepsilon} \cdot \mathbb{S}^{-1}[\boldsymbol{\varepsilon}] \end{aligned} \tag{B.3}$$

at $(\boldsymbol{\varepsilon}, \mathbb{S})$ in direction $(\boldsymbol{\xi}, \mathbb{L})$ computes as

$$\begin{aligned} &\mathrm{D}^2 w_e(\boldsymbol{\varepsilon}, \mathbb{S})[\boldsymbol{\xi}, \mathbb{L}] \\ &= \frac{1}{2}\frac{\mathrm{d}^2}{\mathrm{d}\lambda^2}\left(\frac{1}{2}(\boldsymbol{\varepsilon}+\lambda\boldsymbol{\xi}) \cdot (\mathbb{S}+\lambda\mathbb{L})^{-1}[\boldsymbol{\varepsilon}+\lambda\boldsymbol{\xi}]\right)\Big|_{\lambda=0} \\ &= \frac{1}{2}\frac{\mathrm{d}}{\mathrm{d}\lambda}\left(\boldsymbol{\xi} \cdot (\mathbb{S}+\lambda\mathbb{L})^{-1}[\boldsymbol{\varepsilon}+\lambda\boldsymbol{\xi}] - \frac{1}{2}(\boldsymbol{\varepsilon}+\lambda\boldsymbol{\xi}) \cdot (\mathbb{S}+\lambda\mathbb{L})^{-1}\mathbb{L}(\mathbb{S}+\lambda\mathbb{L})^{-1}[\boldsymbol{\varepsilon}+\lambda\boldsymbol{\xi}]\right)\Big|_{\lambda=0} \\ &= -\frac{1}{2}\boldsymbol{\xi} \cdot \mathbb{S}^{-1}\mathbb{L}\mathbb{S}^{-1}[\boldsymbol{\varepsilon}] + \frac{1}{2}\boldsymbol{\xi} \cdot \mathbb{S}^{-1}[\boldsymbol{\xi}] - \frac{1}{2}\boldsymbol{\varepsilon} \cdot \mathbb{S}^{-1}\mathbb{L}\mathbb{S}^{-1}[\boldsymbol{\xi}] + \frac{1}{2}\boldsymbol{\varepsilon} \cdot \mathbb{S}^{-1}\mathbb{L}\mathbb{S}^{-1}\mathbb{L}\mathbb{S}^{-1}[\boldsymbol{\varepsilon}] \\ &= \frac{1}{2}\boldsymbol{\xi} \cdot \mathbb{S}^{-1}[\boldsymbol{\xi}] - \boldsymbol{\xi} \cdot \mathbb{S}^{-1}\mathbb{L}\mathbb{S}^{-1}[\boldsymbol{\varepsilon}] + \frac{1}{2}\boldsymbol{\varepsilon} \cdot \mathbb{S}^{-1}\mathbb{L}\mathbb{S}^{-1}\mathbb{L}\mathbb{S}^{-1}[\boldsymbol{\varepsilon}] \\ &= \frac{1}{2}(\boldsymbol{\xi} - \mathbb{L}\mathbb{S}^{-1}[\boldsymbol{\varepsilon}]) \cdot \mathbb{S}^{-1}\left[\boldsymbol{\xi} - \mathbb{L}\mathbb{S}^{-1}[\boldsymbol{\varepsilon}]\right]. \end{aligned} \tag{B.4}$$

Appendix C: Extraction tensors based on Puck's theory

Case II: Normal loading perpendicular to fiber direction

As presented in equation (3.6), we define the extraction tensor for case II via

$$\mathbb{B}_{\mathrm{II}} = \frac{1}{2\pi}\int_0^{2\pi} \boldsymbol{n}(\theta)^{\otimes 4}\,\mathrm{d}\theta \quad \text{with} \quad \boldsymbol{n}(\theta) \perp \boldsymbol{e}_1. \tag{C.1}$$

In terms of an orthonormal basis $\{\boldsymbol{e}_1, \boldsymbol{e}_2, \boldsymbol{e}_3\}$ with the $\boldsymbol{e}_1$-axis aligned to the fiber direction, the direction $\boldsymbol{n}$ and the unit vector $\boldsymbol{e}_1$ are $\boldsymbol{n}(\theta) \mathrel{\hat{=}} (0, \cos\theta, \sin\theta)$ and $\boldsymbol{e}_1 \mathrel{\hat{=}} (1, 0, 0)$. We can evaluate the integration for each component of the extraction tensor separately. As $\boldsymbol{n} \perp \boldsymbol{e}_1$, all components of $\mathbb{B}_{\mathrm{II}}$ with at least one index" 1" are zero. The remaining components are

$$B^{\mathrm{II}}_{2222} = \frac{1}{2\pi}\int_0^{2\pi} \cos^4\theta\,\mathrm{d}\theta = \frac{3}{8}, \tag{C.2}$$

$$B^{\mathrm{II}}_{2233} = \frac{1}{2\pi}\int_0^{2\pi} \cos^2\theta \sin^2\theta \,\mathrm{d}\theta = B^{\mathrm{II}}_{3322} = B^{\mathrm{II}}_{2323} = B^{\mathrm{II}}_{2332} = B^{\mathrm{II}}_{3232} = B^{\mathrm{II}}_{3223} = \frac{1}{8}, \tag{C.3}$$

$$B^{\mathrm{II}}_{3333} = \frac{1}{2\pi}\int_0^{2\pi} \sin^4\theta \,\mathrm{d}\theta = \frac{3}{8}, \tag{C.4}$$

$$B^{\mathrm{II}}_{2223} = \frac{1}{2\pi}\int_0^{2\pi} \cos^3\theta \sin\theta \,\mathrm{d}\theta = B^{\mathrm{II}}_{2232} = B^{\mathrm{II}}_{2322} = B^{\mathrm{II}}_{3222} = 0, \tag{C.5}$$

$$B^{\mathrm{II}}_{3332} = \frac{1}{2\pi}\int_0^{2\pi} \cos\theta \sin^3\theta \,\mathrm{d}\theta = B^{\mathrm{II}}_{3323} = B^{\mathrm{II}}_{3233} = B^{\mathrm{II}}_{2333} = 0. \tag{C.6}$$

Hence, the extraction tensor for case II has the form

$$\mathbb{B}_{\mathrm{II}} = \frac{1}{4}(\boldsymbol{e}_2^{\otimes 2} + \boldsymbol{e}_3^{\otimes 2})^{\otimes 2} + \frac{1}{8}(\boldsymbol{e}_2^{\otimes 2} - \boldsymbol{e}_3^{\otimes 2})^{\otimes 2} + \frac{1}{2}(\boldsymbol{e}_2 \otimes_{\mathrm{S}} \boldsymbol{e}_3)^{\otimes 2} \tag{C.7}$$

as presented in (3.7). The composition of the extraction tensor with itself is

$$\mathbb{B}_{\mathrm{II}}^2 = \frac{1}{8}(\boldsymbol{e}_2^{\otimes 2} + \boldsymbol{e}_3^{\otimes 2})^{\otimes 2} + \frac{1}{32}(\boldsymbol{e}_2^{\otimes 2} - \boldsymbol{e}_3^{\otimes 2})^{\otimes 2} + \frac{1}{8}(\boldsymbol{e}_2 \otimes_{\mathrm{S}} \boldsymbol{e}_3)^{\otimes 2}. \tag{C.8}$$

Case III: Shear loading perpendicular to fiber direction

Based on analogous ideas as for case II, we define the extraction tensor (3.11) for case III via an integration over all possible directions in the $\boldsymbol{e}_2$-$\boldsymbol{e}_3$-plane perpendicular to the fiber direction $\boldsymbol{e}_1$

$$\mathbb{B}_{\mathrm{III}} = \frac{1}{2\pi}\int_0^{2\pi} (\boldsymbol{n}(\theta) \otimes_{\mathrm{S}} \boldsymbol{m}(\theta))^{\otimes 2} \,\mathrm{d}\theta \quad \text{with} \quad \boldsymbol{n}(\theta) \perp \boldsymbol{m}(\theta) \perp \boldsymbol{e}_1. \tag{C.9}$$

With respect to the basis $\{\boldsymbol{e}_1, \boldsymbol{e}_2, \boldsymbol{e}_3\}$, the directions $\boldsymbol{n}$ and $\boldsymbol{m}$ are defined as $\boldsymbol{n} \mathrel{\hat{=}} (0, \cos\theta, \sin\theta)$ and $\boldsymbol{m} \mathrel{\hat{=}} (0, -\sin\theta, \cos\theta)$. We can evaluate the integration for each component of the extraction tensor separately. As $\boldsymbol{n} \perp \boldsymbol{m} \perp \boldsymbol{e}_1$ and $n_1 = m_1 = 0$, all components with at least one index" 1" are zero. For the remaining components we get

$$B^{\mathrm{III}}_{2222} = \frac{1}{2\pi}\int_0^{2\pi} \cos^2\theta \sin^2\theta \,\mathrm{d}\theta = \frac{1}{8}, \tag{C.10}$$

$$B^{\mathrm{III}}_{2233} = -\frac{1}{2\pi}\int_0^{2\pi} \sin^2\theta \cos^2\theta \,\mathrm{d}\theta = B^{\mathrm{III}}_{3322} = -\frac{1}{8}, \tag{C.11}$$

$$B^{\mathrm{III}}_{2323} = \frac{1}{2\pi}\int_0^{2\pi} \frac{1}{4}(\sin^4\theta + \cos^4\theta - 2\sin^2\theta\cos^2\theta) \,\mathrm{d}\theta = B^{\mathrm{III}}_{2332} = B^{\mathrm{III}}_{3232} = B^{\mathrm{III}}_{3223} = \frac{1}{8}, \tag{C.12}$$

$$B^{\mathrm{III}}_{3333} = \frac{1}{2\pi}\int_0^{2\pi} \sin^2\theta \cos^2\theta \,\mathrm{d}\theta = \frac{1}{8}, \tag{C.13}$$

$$B^{\mathrm{III}}_{2223} = \frac{1}{4\pi}\int_0^{2\pi} \left(\sin^3\theta\cos\theta - \sin\theta\cos^3\theta\right) \mathrm{d}\theta = B^{\mathrm{III}}_{2232} = B^{\mathrm{III}}_{2322} = B^{\mathrm{III}}_{3222} = 0, \tag{C.14}$$

$$B^{\mathrm{III}}_{3332} = \frac{1}{4\pi}\int_0^{2\pi} \left(\sin\theta\cos^3\theta - \sin^3\theta\cos\theta\right) \mathrm{d}\theta = B^{\mathrm{III}}_{3323} = B^{\mathrm{III}}_{3233} = B^{\mathrm{III}}_{2333} = 0. \tag{C.15}$$

As presented in (3.12), the extraction tensor for case III therefore has the form

$$\mathbb{B}_{\mathrm{III}} = \frac{1}{8}\left(\boldsymbol{e}_2^{\otimes 2} - \boldsymbol{e}_3^{\otimes 2}\right)^{\otimes 2} + \frac{1}{2}\left(\boldsymbol{e}_2 \otimes_{\mathrm{S}} \boldsymbol{e}_3\right)^{\otimes 2}. \tag{C.16}$$

The composition of the extraction tensor with itself is

$$\mathbb{B}^2_{\mathrm{III}} = \frac{1}{4}\mathbb{B}_{\mathrm{III}}. \tag{C.17}$$

Case IV: Shear loading in fiber direction

In analogy to case II and case III we define the corresponding extraction tensor (3.16) for case IV as

$$\mathbb{B}_{\mathrm{IV}} = \frac{1}{2\pi}\int_0^{2\pi} \left(\boldsymbol{n}(\theta) \otimes_{\mathrm{S}} \boldsymbol{e}_1\right)^{\otimes 2} \mathrm{d}\theta \quad \text{with} \quad \boldsymbol{n}(\theta) \perp \boldsymbol{e}_1 \tag{C.18}$$

Again, we can evaluate the integration for each component of the extraction tensor separately. The directions are defined as $\boldsymbol{n} \hat{=} (0, \cos\theta, \sin\theta)$ and $\boldsymbol{e}_1 \hat{=} (1, 0, 0)$, with $\boldsymbol{n} \perp \boldsymbol{e}_1$. Hence, the only non-zero components are B_{2121}, B_{2112}, B_{1221}, B_{1212}, B_{3131}, B_{3113}, B_{1331} and B_{1313}. These components are computed as

$$B^{\mathrm{IV}}_{2121} = \frac{1}{8\pi}\int_0^{2\pi} \cos^2\theta \, \mathrm{d}\theta = B^{\mathrm{IV}}_{2112} = B^{\mathrm{IV}}_{1221} = B^{\mathrm{IV}}_{1212} = \frac{1}{8}, \tag{C.19}$$

$$B^{\mathrm{IV}}_{3131} = \frac{1}{8\pi}\int_0^{2\pi} \sin^2\theta \, \mathrm{d}\theta = B^{\mathrm{IV}}_{3113} = B^{\mathrm{IV}}_{1331} = B^{\mathrm{IV}}_{1313} = \frac{1}{8}. \tag{C.20}$$

The extraction tensor for case IV therefore has the presented form (3.17)

$$\mathbb{B}_{\mathrm{IV}} = \frac{1}{2}\left(\boldsymbol{e}_1 \otimes_{\mathrm{S}} \boldsymbol{e}_2\right)^{\otimes 2} + \frac{1}{2}\left(\boldsymbol{e}_1 \otimes_{\mathrm{S}} \boldsymbol{e}_3\right)^{\otimes 2}. \tag{C.21}$$

The composition of the extraction tensor with itself is

$$\mathbb{B}^2_{\mathrm{IV}} = \frac{1}{4}\mathbb{B}_{\mathrm{IV}}. \tag{C.22}$$